Geotextiles and Geomembranes 51 (2023) 342–359

Contents lists available at ScienceDirect

Geotextiles and Geomembranes

journal homepage: www.elsevier.com/locate/geotexmem

Regular Paper

Model tests of geosynthetic-reinforced soil walls with marginal backfill subjected to rainfall

Kuo-Hsin Yang [a,*], Hsin-Ming Wu [b], Ting-Ling Tseng [b], Chungsik Yoo [c]

[a] Department of Civil Engineering, National Taiwan University (NTU), 1, Sec. 4, Roosevelt Rd., Taipei, 106, Taiwan
[b] Department of Civil Engineering, National Taiwan University, Taiwan
[c] School of Civil and Architectural Engineering, Sungkyunkwan University, South Korea

ARTICLE INFO

Keywords:
Geosynthetics
GRS wall
Marginal backfill
Rainfall
Sand cushion

ABSTRACT

A series of model tests were conducted to investigate the performance of geosynthetic-reinforced soil (GRS) walls with marginal backfill subjected to rainfall infiltration. The effectiveness of improvement measures—such as decreasing reinforcement spacing and increasing sand cushion thickness—to prevent the GRS wall failure due to heavy rainfall was evaluated. The distribution and variation of the volumetric water content, porewater pressure, wall deformation, and reinforcement tensile strain were monitored during the test. The advancement of the wetting front and the drainage function of sand cushions were visually observed using the fluorescent dyeing technique. For the baseline case, the wall began to deform as rainfall proceeded, causing the potential failure surface to gradually move backward. When the potential failure surface moved beyond the reinforced zone, the pullout of the topmost reinforcement layers occurred, resulting in the collapse of the GRS wall in a compound failure mode. Decreases in reinforcement spacing and increases in sand cushion thickness effectively reduced wall deformation and enhanced wall stability. The placing of sand cushions between the reinforcement layers can also delay water infiltration and reduce the accumulation of porewater pressure inside the wall. Suggestions for designing rain-resistant GRS walls are also proposed based on the findings.

1. Introduction

Geosynthetic-reinforced soil (GRS) structures have been widely used in practice for construction applications. Moreover, GRS structures that perform successfully during natural disasters, such as earthquakes, fault movements, floods, tsunamis, landslides, rock falls, debris flows, and avalanches, have been reported in the literature (Brandl, 2011; Fowze et al., 2012; Koseki and Shibuya, 2014; Kuwano et al., 2012; Lambert and Bourrier, 2013; Saran and Viswanadham 2018; Recio-Molina and Yasuhara, 2005; Yang et al., 2020; Yasuhara and Recio-Molina, 2007). However, studies have also observed the failure of GRS structures, particularly those backfilled with marginal soil under heavy rainfall (Hadded and Shafabakhsh 2008; Hossain et al., 2012; Kim and Borden 2013; Leonards et al., 1994; Liu et al., 2012; Mitchell and Zornberg 1995; Miyata and Shinoda 2016; Scarborough 2005; Shibuya et al., 2007, 2011; Wu and Tang 2008; Yang et al., 2019a; Yoo and Jung 2006). The failures of GRS structures were mainly due to rainfall infiltration or groundwater seepage, the use of marginal backfill containing excessive fines (typically with low permeability), insufficient compaction, and malfunctioning drainage systems, as summarized from the past studies (Koerner and Koerner 2013, 2018; Wu and Chou 2013; Valentine 2013).

Although granular soil is recommended as a backfill material for GRS structures in design guidelines, in-situ soils containing fines (referred to as marginal backfill) have often been adopted as alternative backfills due to the economic and sustainable benefits (i.e., minimized transportation costs and the environmental impact) if granular backfill is not readily available on site. Marginal soils are also used to comply with local environmental regulations stipulating that the excavated and backfilled soils at a construction site should be balanced. Table 1 lists the gradation limits and plasticity index for backfill suggested in design guidelines (AASHTO 2002; Berg et al., 2009; Elias et al., 2001). Soil that satisfies the grain size recommendations specified in the design guidelines (i.e., granular soil) is referred to as good-quality backfill. By contrast, soil that does not meet these recommendations (e.g., cohesive soil) is referred to as marginal backfill. Marginal backfill can compromise the performance of GRS structures upon wetting from rainfall infiltration or groundwater seepage due to the accumulation of porewater pressure (PWP) within backfills (Koerner and Koerner 2013, 2018;

* Corresponding author.
E-mail addresses: khyang@ntu.edu.tw (K.-H. Yang), D07521002@ntu.edu.tw (H.-M. Wu), kobe010494@gmail.com (T.-L. Tseng), csyoo@skku.edu (C. Yoo).

https://doi.org/10.1016/j.geotexmem.2022.12.002
Received 27 June 2022; Received in revised form 3 December 2022; Accepted 12 December 2022
Available online 30 December 2022

Table 1
Backfill properties for GRS structures suggested in design guidelines.

Item	Symbol	Wall ($\beta \geq 70°$)	Slope ($\beta < 70°$)
Maximum particle size (mm)	D_{max}	$\leq$ 125 mm	$\leq$ 100 mm
Percent passing (%)	4.75 mm (No. 4)	0–100	20–100
	0.425 mm (No. 40)	0–60	0–60
	0.075 mm (No. 200)	0–15	0–50
Plasticity Index (%)	PI	$\leq$ 6	$\leq$ 20

Note: β is the wall inclination angle.

Mamaghanian et al., 2019; Mitchell and Zornberg 1995; Razeghi et al., 2019; Valentine 2013; Viswanadham et al., 2017; Yoo and Jung 2006; Zornberg and Arriaga, 2003). Therefore, the performance and design of GRS structures with marginal backfill during rainfall are key issues that deserve special attention.

Studies have conducted numerical simulations to evaluate the performance and failure mechanisms of GRS structures under rainfall (Albino et al., 2020; Bhattacherjee and Viswanadham 2015; Fox 2022; Jayanandan and Viswanadham 2019; Nunes et al., 2022; Thuo et al., 2015; Vahedifard et al., 2016, 2017; Yang et al., 2018, 2019b). These numerical studies have incorporated the framework of unsaturated soil mechanics to model the hydraulic and mechanical responses of GRS structures when the soil transitions from unsaturated to saturated conditions due to rainfall infiltration. Their numerical results have indicated that as the rainfall-induced wetting front advances, the soil loses its matric suction and develops positive PWP, and thus the stability of GRS structures decreases. Few studies have performed model tests on GRS structures subjected to rainfall (Bhattacherjee and Viswanadham, 2019; Garcia et al., 2007; Iryo and Rowe 2005; Portelinha et al., 2013, 2021; Portelinha and Zornberg 2017; Ren et al., 2022; Yoo et al., 2022; Yoo and Jang 2013). These experimental studies have mainly (1) investigated the variation of wall deformation, mobilized reinforcement tensile force, and PWP during rainfall (2) evaluated the effect of installing the drainage system on the performance of GRS structures. Among these experimental studies, only one study (Bhattacherjee and Viswanadham 2019) tested GRS structures to failure. The failure process and mechanism of GRS structures upon rainfall must be further investigated to understand the development of failure surfaces and failure modes due to rainfall.

The drainage system, including back vertical and internal horizontal drains, plays an important role in the performance of GRS structures. Past studies have demonstrated that installing the drainage system could effectively decrease PWP within the backfill and increase the system stability (Chinkulkijniwat et al., 2016; Koerner and Koerner, 2011; Mamaghanian et al., 2019; Razeghi et al., 2019; Viswanadham et al., 2017; Yoo et al., 2022). In this study, sand cushions (granular soil layers sandwiching the reinforcement layers) were used as alternative drain layers. The effectiveness of sand cushions in reducing PWP within the backfill and lowering the phreatic surface level was evaluated experimentally in this study. Sand cushions have been demonstrated to effectively improve the mechanical and hydraulic behavior of marginal soil (Abdi et al., 2009; Abdi and Zandieh 2014; Balakrishnan and Viswanadham 2019; Chen and Yu 2011; Lin and Yang 2014; Raisinghani and Viswanadham 2010, 2011; Thuo et al., 2015; Unnikrishnan et al., 2002; Yang et al., 2016, 2018). These studies have demonstrated that placing sand cushions in marginal soil yields the following advantages: it (1) accelerates PWP dissipation in soil saturated conditions, (2) reduces the capillary barrier effect in soil unsaturated conditions, (3) mitigates the surficial intrusion and long-term clogging in nonwoven geotextiles by fine-grained soils, (4) enhances pullout resistance by improving the soil–reinforcement interface shear strength, and (5) improves the strength and deformation characteristics of reinforced clay. However, these findings are mainly based on soil specimen tests or numerical simulations. Limited studies evaluating the overall performance of GRS structures with sand cushions have been published. In Balakrishnan and Viswanadham (2019), the GRS wall centrifuge models were constructed with marginal backfill placed at the wet of optimum water content (OMC +5%) to simulate the wet soil conditions. No other external water source (i.e., seepage or rainfall) was applied during centrifuge tests. The reinforcement spacing S_v (= 0.148H) and thickness of sand cushion t_{sc} (= 0.25S_v) are constant for all centrifuge tests. They concluded that the sand cushion provided a greater pullout resistance along the soil-reinforcement interface, which reduced the straining of geogrid reinforcement layers, and limited the surface settlements and face movements of geogrid-reinforced soil wall.

This study presents a series of model tests to investigate the performance of GRS walls with marginal backfill subjected to rainfall. The main objectives are to (1) evaluate the performance of GRS walls with marginal backfills subjected to rainfall, (2) assess the effectiveness of various reinforcement spacings and sand cushion thicknesses for improving the drainage and stability of GRS walls, and (3) provide design suggestions for improving the resistance of GRS structures to rainfall. Notably, Balakrishnan and Viswanadham (2019) only evaluated the mechanical function of the sand cushion in improving reinforcement pullout resistance. In this study, both the mechanical and hydraulic functions of the sand cushion in improving pullout resistance and drainage capacity of the wall system were evaluated. The remaining parts of the paper proceed as follows. First, the reduced model tests conducted in the study are introduced. Second, the soil and reinforcement materials, model preparation, test procedure, and digital image analysis (DIA) techniques are described. Third, the test results for the volumetric water content (VWC), PWP, wall facing displacement, failure surface, and mobilized reinforcement tensile strain are then presented. In addition, visual observations made with the fluorescent dyeing technique are described with regard to the advancement of the wetting front due to rainfall and the drainage function of sand cushions. The results of this study provide insightful information for the analysis and design of GRS structures with marginal backfill to better withstand the negative effects of rainfall.

2. Experimental program

2.1. Reduced model and test program

The reduced model tests on GRS walls were conducted using a sandbox in the geotechnical research laboratory at National Taiwan University. The similitude law for the 1-g model test is carefully considered to replicate the mechanical response of a field prototype structure in a reduced-scale model test, as discussed in the corresponding section. Fig. 1 presents the test setup, and Fig. 2 illustrates the detailed layout and instrumentation of the wall model. The dimensions of the sandbox were 100 cm × 30 cm × 90 cm (length × width × height). A transparent Plexiglas wall was installed on the front side to visually observe and record wall deformation during the test. The inner surface of the sandbox was carefully treated to minimize the side friction at the soil-sandbox interface. According to Liu et al. (2014), the application of silicon spray lubricant sandwiched between two polyethylene (PE) sheets at the soil-sandbox interface can yield an 80% reduction in interface friction relative to the interface friction angle for direct contact (i.e., without treatment). The same method was adopted in this study to reduce the effect of side friction and maintain the model test under plane strain conditions.

The wall model comprised a reinforced zone, retained zone, and foundation. The total height (H) and length of the wall were 60 and 77 cm, respectively (Fig. 2). According to the similitude laws for the 1-g physical model test (Baker et al., 1991; Muir-Wood, 2004), this wall height is equivalent to 3 m in a prototype for the target scaling factor N = 5 selected in this study. In the reinforced zone, the reinforcement had length L = 42 cm; thus, a wall aspect ratio of L/H = 0.7 as recommended in design guidelines is achieved (AASHTO 2002; Berg et al., 2009; Elias et al., 2001). The wall facing comprised a 2-cm sand filter layer

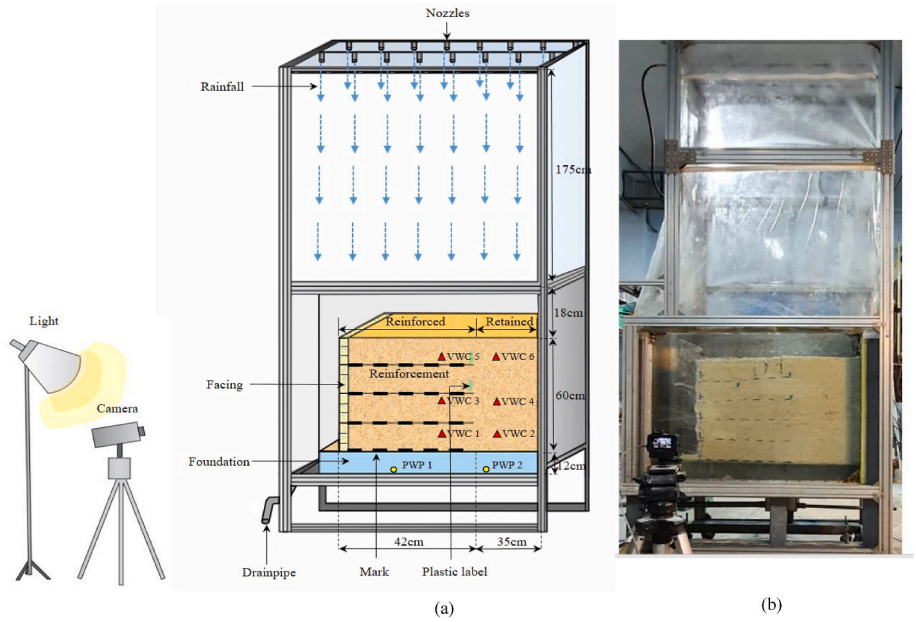

Fig. 1. Test setup and sandbox: (a) illustration; (b) photo.

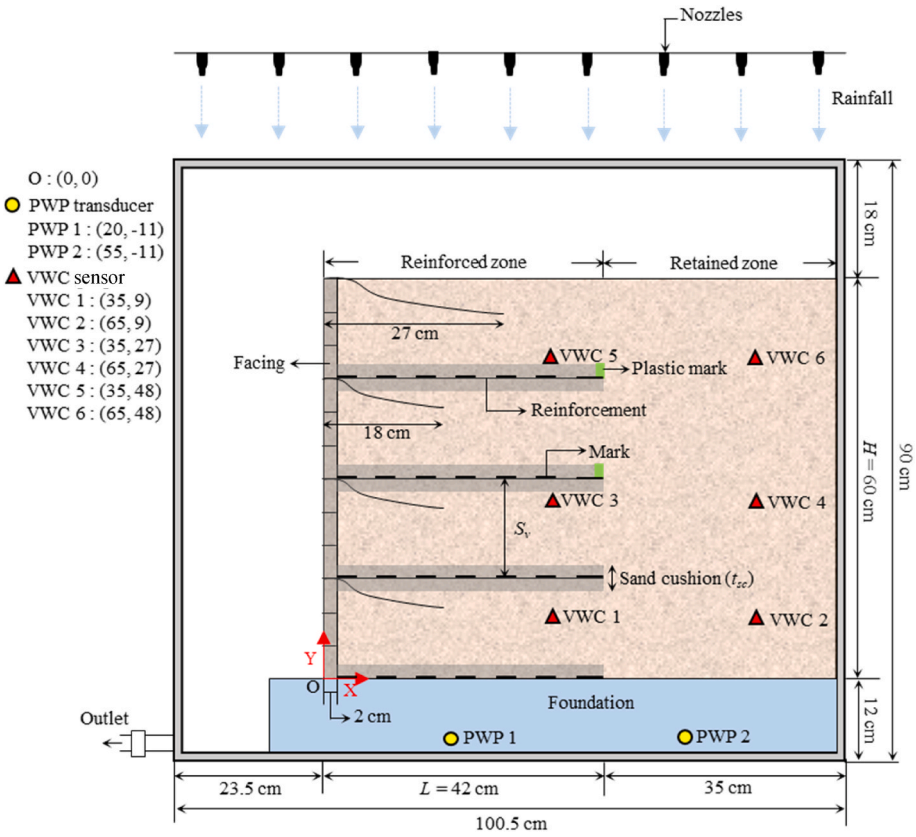

Fig. 2. Detailed layout and instrumentation of the GRS wall model.

encapsulated by the reinforcement wrap-around. The sand filter layer simulates sandbags used in practical construction to prevent the loss of backfill, especially for those containing fines. The length of the wrap-around (or secondary) layer was 18 cm (≈0.45 × L); however, a longer wrap-around length was used for the topmost layer to prevent it from pulling out (or flipping over) during the test due to the low overburden pressure. The retained zone had a length of 35 cm, which permits the development of a compound failure mode (i.e., the failure surface passing through both the reinforced and retained zone). The foundation was an acrylic tank. The top of the foundation was perforated with a series of small holes and covered by a permeable nonwoven geotextile as a filter to prevent soil loss. The acrylic tank was filled with water at the end of the wall construction to simulate a firm foundation with a high groundwater level.

Rainfall was simulated with an irrigation system installed approximately 2 m above the wall. The irrigation system comprises two rows of nozzles with eight nozzles on each row (Fig. 3a). A pressurized motor connected to a faucet pumped water to the nozzles. The rainfall droplets sprayed from the nozzles were smaller than 0.1 mm. This fine spray ensures that droplets achieve low terminal velocity before falling on the GRS wall and thus do not erode the crest. A rainfall intensity of $I = 75$ mm/h was used in the tests to simulate an intense precipitation event, such as a typhoon or heavy rain. To ensure a uniform distribution of rainwater over the top surface of the wall, thirty transparent boxes (Fig. 3b) were placed inside the sandbox to collect the rainwater. The rainfall uniformity is determined as follows:

$$U_c = 1 - \frac{\sum|x_i - \bar{x}|}{\sum x_i} \quad (1)$$

where U_c is the rainfall uniformity, x_i is the rainwater collected in the ith box, and $\bar{x}$ is the average rainwater value from all the boxes. The test results indicated the irrigation system used in this study achieved $U_c >$ 90%, suggesting the irrigation system produced simulated rainfall with a reasonably high uniformity.

Table 2 summarizes the experimental test program. A total of seven reduced model tests were performed to explore the effect of reinforcement spacing and sand cushion thickness on the performance of GRS walls subjected to rainfall. For the test series with different reinforcement spacings, "SM" denotes the silty sand used as backfill and the subsequent number denotes the reinforcement spacing in centimeters. For the test series with different sand cushion thicknesses, "SC" denotes sand cushion and the subsequent number denotes the thickness of the sand cushion in centimeters. For example, Test SM15+SC4 represents a wall model backfilled with silty sand with a reinforcement spacing of 15 cm; each reinforcement was sandwiched by a 4-cm sand cushion (2 cm on top of and 2 cm below the reinforcement layer) (Fig. 2). For a vertical reinforcement spacing of 15 cm, the use of 2-, 4-, and 6-cm sand cushions are equivalent to replacing 11.6%, 23%, and 35% of the volume of marginal backfill with sand, respectively. Table 2 also lists the factor of safety (FS) values for internal stability against reinforcement breakage and pullout calculated based on design guidelines (AASHTO 2002; Elias et al., 2001). The FS values under normal (as-compacted) conditions were calculated using the as-compacted soil shear strength properties. The FS values under rainfall conditions were calculated using the saturated soil shear strength properties and under the assumption that the phreatic surface level increased to the midheight of the wall. For the cases with sand cushions, as illustrated in Fig. 4, the lateral earth pressure distribution was calculated considering the active earth pressures for the silty sand and sand cushions at the corresponding depths.

2.2. Material properties

Two soils, silty sand and quartz sand, and one geogrid reinforcement were used in the experimental tests. Table 3 summarizes the soil and reinforcement properties obtained from laboratory tests. Fig. 5 presents the soil grain size distribution curves. Silty sand, comprising 80% sand mixed with 20% kaolin by weight, was used as backfill. The silty sand had a specific gravity $G_s = 2.62$, plastic limit PL = 6, liquid limit LL = 13, plasticity index PI = 7, and was classified as "SM" according to the Unified Soil Classification System (USCS). The silty sand used in tests is considered as marginal backfill because its fines content F = 20% (>15%) and PI = 7 (>6) exceed the values suggested in the design guidelines (Table 1). The maximum dry unit weight and optimum water content of the silty sand were $\gamma_{d,max}$ = 18.1 kN/m^3 and ω_{opt} = 10.7%, respectively, according to results from standard Proctor compaction tests (ASTM-D698). The silty sand at the target density had effective friction angles φ' = 34.6° and 30.5° under as-compacted and saturated conditions, respectively, and negligible cohesion under both conditions based on the direct shear test results (ASTM-D3080). The saturated hydraulic conductivity of the silty sand was $k = 5.72 \times 10^{-6}$ m/s, as determined by falling head tests (ASTM-D5084).

Quartz sand was used for the facing filter and the sand cushion. The quartz sand had G_s = 2.65, mean particle size D_{50} = 0.25 mm, and was classified as "SP" according to the USCS. The maximum and minimum dry unit weights of the sand were $\gamma_{d,max}$ = 15.21 kN/m^3 and $\gamma_{d,min}$ = 13.54 kN/m^3, respectively (ASTM-D4253 and D4254). The sand at the target density had φ' = 37.3° and 33.7° under as-compacted and saturated conditions, respectively, based on the direct shear test results. The saturated hydraulic conductivity of the sand was $k = 5.3 \times 10^{-4}$ m/s, as determined using constant head tests (ASTM-D2434). Notably, the hydraulic conductivity of the sand is approximately two orders of magnitude greater than that of the silty sand.

The geogrid reinforcement used in the tests was from a commercial

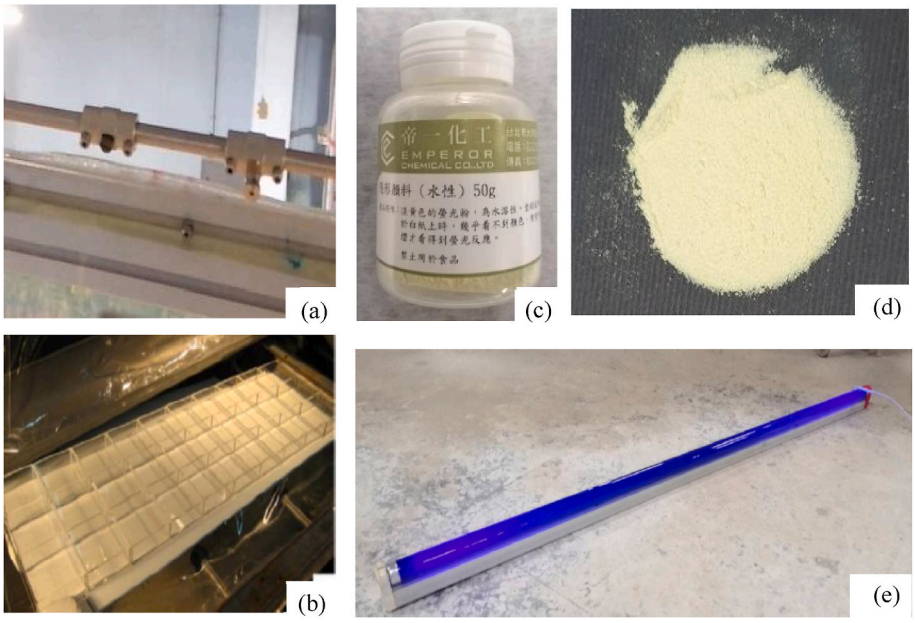

Fig. 3. Test devices (a) irrigation nozzles; (b) transparent boxes to determine the uniformity of the applied rainfall; (c), (d) water-soluble fluorescent dye powder; (e) UV lamp.

Table 2
Test program and factor of safety of internal design.

Test variables	Test ID	Reinforcement spacing (cm)	Number of reinforcement layers	Thickness of sand cushions (cm)	Normal (as-compacted)		Rainfall	
					$FS_{breakage}$	$FS_{pullout}$	$FS_{breakage}$	$FS_{pullout}$
Spacing	SM 20	20 (100)	3	0	3.30	3.03	2.19	1.94
	SM 15	15 (75)	4	0	3.91	3.53	2.29	2.20
	SM 12	12 (60)	5	0	4.59	4.04	2.58	2.46
	SM 10	10 (50)	6	0	5.28	4.54	2.91	2.73
Sand cushion	SM 15+SC 2	15 (75)	4	2 (10)	4.01	3.64	2.30	2.45
	SM 15+SC 4	15 (75)	4	4 (20)	4.12	3.71	2.38	2.49
	SM 15+SC 6	15 (75)	4	6 (30)	4.22	3.79	2.44	2.53

Note: the values in prototype are indicated in the parenthesis. Test SM15 is the baseline case.

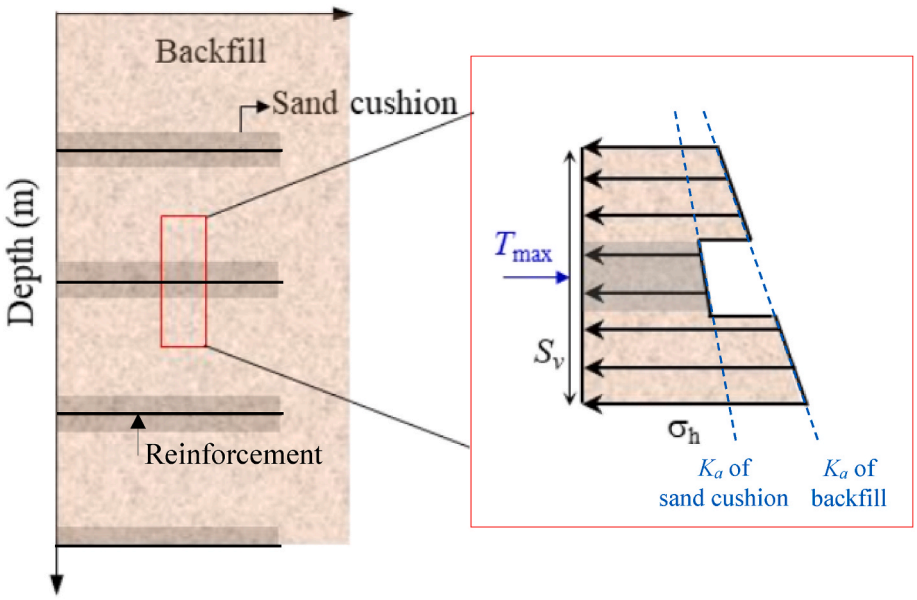

Fig. 4. Assumed lateral earth pressure distribution diagram of the GRS wall with sand cushion.

polyester washnet bag. The selected geogrid had a mass per unit area of 14.08 g/m^2 and hexagonally shaped apertures with an average aperture size of 2 mm. The ratio of the geogrid aperture size to the mean particle size of the backfill soil was $s_g/D_{50} = 10$, which falls within the range $7 < s_g/D_{50} < 12$ for optimum soil–geogrid interactions suggested by Mohammad and Parastoo (2017). Fig. 6 presents the tensile force–strain response of the geogrid obtained from wide-width tensile tests (ASTM-D4595). The ultimate tensile strength and the corresponding strain were $T_{ult} = 1.23$ kN/m and $\varepsilon_f = 16.68\%$, respectively. The secant stiffness at 2% strain and at failure were $J_{2\%} = 6$ kN/m and $J = 7.36$ kN/m, respectively. The soil–reinforcement interface properties were determined using an apparatus modified from a conventional direct shear box. The modified direct shear box comprised an upper shear box filled with the test soil and a lower shear box containing a steel block that acted as an even shear surface. The geogrid was placed on top of the lower shear box and fixed to two sides with screws to prevent the geogrid from moving during the test. Table 4 summarizes the soil–reinforcement interface properties under both as-compacted and saturated conditions. The efficiency factor E_τ is listed in Table 4 and is defined as follows:

$$E_\tau = \frac{\tan\delta}{\tan\varphi'} \tag{2}$$

where δ is the interface friction angle, and φ' is the effective friction angle. The test results in Table 4 reveal that δ for the silty sand–geogrid interface decreased by approximately 15% when the interface changed from being as-compacted to saturated.

Table 5 lists the scaling factors and corresponding prototype values for the selected geogrid in this study. According to the similitude law for the 1-g model test, the ultimate tensile strength and stiffness of the reinforcement in the model test should be scaled down to $1/N^2$, where N is the target scaling factor for geometry (i.e., $N = 5$ in this study). These scaling factors for the reinforcement properties were derived from the Buckingham π theorem (Buckingham 1914). Past studies on the model tests of GRS walls have also adopted the same scaling factors (Garcia et al., 2007; Guo et al., 2022; Viswanadham and König 2004; Yasuhara and Recio-Molina 2007; Yoo et al., 2022). The prototype tensile properties of the selected geogrid fall within the typical ranges (J = 120–5000 kN/m, and T_{ult} = 12–1000 kN/m) of prototype geosynthetic reinforcements used in GRS walls (Allen and Bathurst 2019; Bathurst and Naftchali 2021).

2.3. Model preparation and test procedure

The wall model had a total height of 60 cm; it was constructed by backfilling and compacting the silty sand in several lifts to achieve a uniform density. For each 5-cm lift, a calculated weight of the silty sand was carefully mixed with the optimum water content ($\omega_{opt} = 10.7\%$), and then evenly distributed in the sandbox. The silty sand was then compacted using a 15 cm × 15 cm steel hammer. After the compaction was completed, the soil surface was scarified prior to the addition of the next soil lift to increase interfacial bonding with the overlying material. The sand was filled within a distance of 2 cm from the wall facing to

Table 3
Soil and reinforcement properties.

Properties	Value
Silty sand (Backfill)	
Soil classification (USCS)	SM
Specific gravity, G_s	2.62
Fines content, F (%)	20
Mean grain size, D_{50} (mm)	0.20
Plastic limit, PL	6
Liquid limit, LL	13
Plasticity index, PI	7
Maximum dry unit weight, $\gamma_{d,max}$ (kN/m^3)	18.1
Optimum water content, ω_{opt} (%)	10.7
Target unit weight, γ (kN/m^3)	17.0
Friction angle (as-compacted), φ' (°)	34.6
Friction angle (saturated), φ' (°)	30.5
Saturated hydraulic conductivity, k (m/s)	5.72×10^{-6}
Sand (Facing filter and sand cushion)	
Soil classification (USCS)	SP
Specific gravity, G_s	2.65
Mean grain size, D_{50} (mm)	0.25
Maximum dry unit weight, $\gamma_{d,max}$ (kN/m^3)	15.21
Minimum dry unit weight, $\gamma_{d,min}$ (kN/m^3)	13.54
Target unit weight, γ (kN/m^3)	15.43
Friction angle (as-compacted), φ' (°)	37.3
Friction angle (saturated), φ' (°)	33.7
Saturated hydraulic conductivity, k (m/s)	5.3×10^{-4}
Reinforcement	
Type	Geogrid
Material	Polyester (PET)
Mass per unit area (g/m^2)	14.08
Ultimate tensile strength, T_{ult} (kN/m)	1.23
Failure strain, ε_f (%)	16.68
Stiffness at 2% strain, $J_{2\%}$ (kN/m)	6
Stiffness at failure, J (kN/m)	7.36

form a sand filter layer, simulating the sandbags used in practical construction to prevent the loss of the backfill. Precut Styrofoam bricks were placed in front of the wall as formwork to prop the wall and prevent its movement during the backfilling process. When the design elevation of a reinforcement layer was reached, a geogrid was laid over the soil layer and folded back at the wall facing to form a wrap-around facing. For the tests with sand cushions, a lower sand cushion was placed followed by a geogrid and then an upper sand cushion. The sand was placed carefully

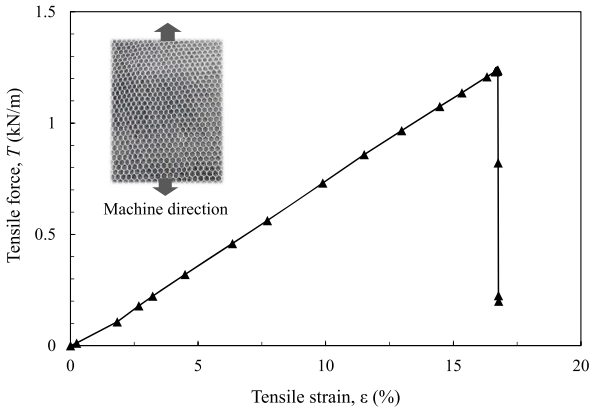

Fig. 6. Wide-width tensile test result of the geogrid.

Table 4
Soil-reinforcement interface properties under as-compact and saturated conditions.

Interface	Condition	Interface friction angle δ (°)	Efficiency factor E_τ
Silty sand-geogrid	As-compacted	29.2	0.81
Silty sand-geogrid	Saturated	25.0	0.80
Sand-geogrid	As-compacted	29.5	0.74
Sand-geogrid	Saturated	27.0	0.76

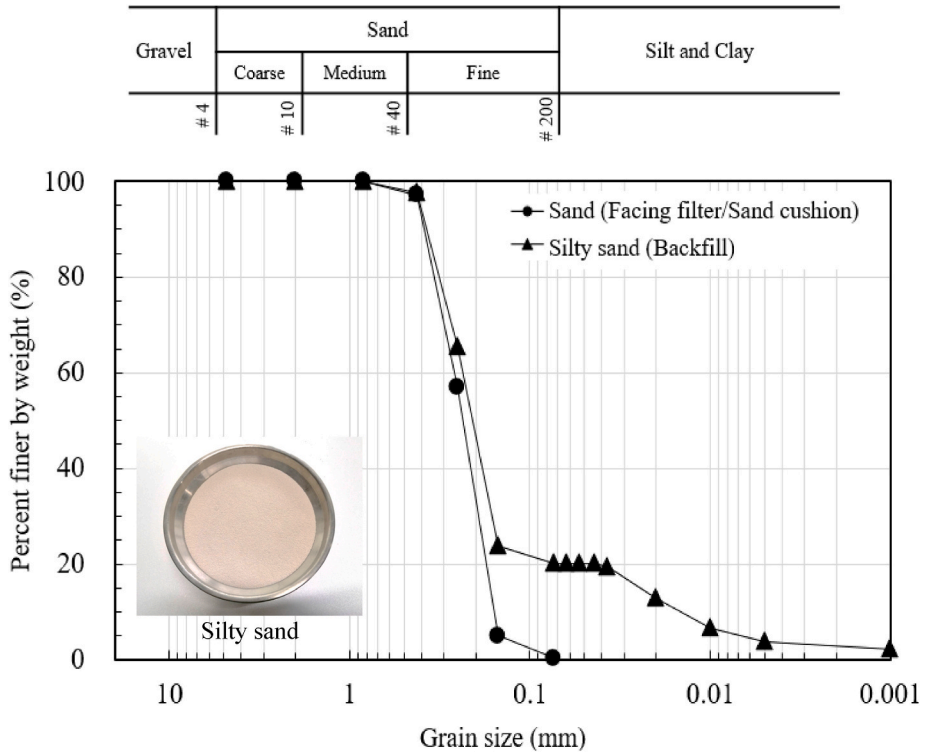

Fig. 5. Grain size distribution curves of backfill and sand cushion.

Table 5
Scaling factors and values based on the similarity requirements.

Parameters	Scaling factor	Model	Prototype
Geometry			
Wall height, H (m)	$1/N$	0.6	3.0
Reinforcement length, L (m)	$1/N$	0.42	2.1
Soil parameter (Backfill)			
Target unit weight, γ (kN/m^3)	1	17.0	17.0
Friction angle (as-compacted), φ' (°)	1	34.6	34.6
Friction angle (Saturated), φ' (°)	1	30.5	30.5
Saturated hydraulic conductivity, k (m/s)	1	5.72×10^{-6}	5.72×10^{-6}
Reinforcement parameter			
Aperture size, s_g (mm)	$1/N$	2	10
Ultimate tensile strength, T_{ult} (kN/m)	$1/N^2$	1.23	30.8
Stiffness at 2% strain, $J_{2\%}$ (kN/m)	$1/N^2$	6	150
Stiffness at failure, J (kN/m)	$1/N^2$	7.36	184
Interface friction angle, δ (°)	1	Table 4	Table 4
Rainfall			
Intensity, I (mm/hr)	1	75	75
Duration, t (min)	$1/N$	85	425

Note: target scaling factor $N = 5$.

to maintain a target relative density of $D_r = 70\%$. Black colored sand was laid above the reinforcements at regular intervals for facilitating the analyses of the reinforcement tensile strain ε with DIA, as is discussed later in the paper (Fig. 2). Plastic markers were attached to the end of the reinforcement layer to serve as an indicator for reinforcement pullout (Fig. 2). This construction process was repeated until the wall model reached the desired height.

After the wall model was completed, rainfall at an intensity of $I = 75$ mm/h was generated. The applied rainfall intensity was much higher than the saturated hydraulic conductivity of the silty sand (i.e., $I \gg k$). The tests were terminated when the wall collapsed or at $t = 85$ min, whichever was earlier. According to the Buckingham π theorem (Buckingham 1914) the scaling factor for t between the tested model and a scaled-up prototype can be determined as follows:

$$\frac{t_m}{t_p} = \frac{\rho_p g_p k_p \mu_m l_m}{\rho_m g_m k_m \mu_p l_p} \tag{3}$$

where ρ is the mass density of the fluid, k is the soil hydraulic conductivity, g is the gravitational acceleration, μ is fluid viscosity, l is the seepage length, and the subscripts "m" and "p" indicate the model and prototype. The values of ρ, k, g, and μ were identical in the prototype and the model for the 1-g model tests for the same fluid and soil, implying the seepage velocity was the same in the prototype and the model. For the scaling factor N, l_m is $1/N$ times l_p; thus, the scaling factor for t is also $1/N$. In other word, t_p is N times longer than t_m because the seepage distance of the prototype is N times larger than that in the model. Thus, for the target scaling factor of $N = 5$, the total rainfall duration of $t = 85$ min in the model is equivalent to $t = 425$ min ($= 85$ min $\times$ 5) in the prototype.

2.4. Instrumentation and digital image analysis

The VWC, PWP, wall deformation, and reinforcement tensile strain were monitored during the test. Six VWC sensors (METER ECH$_2$O EC-5) were placed in the reinforced and retained zones to measure the distribution of soil volumetric water content within the wall model (Fig. 2). The measuring range of the VWC sensors was 0–100% with a resolution of approximately ±0.1%. Two PWP transducers (KYOWA PGM-02KG) were installed at the bottom of the foundation to measure increases in the phreatic surface level within the wall model as rainfall proceeded (Fig. 2). The capacity of the PWP transducers was up to 20 kPa with a resolution of approximately ±0.1 kPa. The PWP transducers were submerged into the water at the beginning of the test by filling the foundation tank with water to ensure their full saturation, enabling stable and accurate measurements of positive PWP.

A high-resolution digital camera (GoPro 6) was aimed at the front side of the sand box to continuously record video of the wall as it deformed. Images from the recorded video were then analyzed using various DIA techniques to observe the wall facing deformation, failure surface development, and reinforcement tensile strain mobilization. To determine the development of the potential failure surface, successive digital images were analyzed using Ncorr (Blaber et al., 2015), a digital image correlation (DIC) software, to obtain the displacement and strain fields of the soil. The DIC analyses were facilitated by seeding black colored sand in the model as tracer particles. The failure surface within the wall model could then be identified as that with the most intense shear strain obtained from the DIC analyses.

The reinforcement tensile strain mobilization was determined using the DIA technique proposed by Zornberg and Arriaga (2003). This technique was also adopted by Balakrishnan and Viswanadham (2016) and Yang et al. (2020) to analyze the mobilized reinforcement tensile strain in the GRS wall model tests. In essence, a sigmoid function was fit to the accumulated displacement curve of the reinforcement (Eq. (4)). The tensile strain distribution of the reinforcement was then calculated from the derivative of the sigmoid function with respect to the distance from the wall face x (Eq. (5)).

$$d(x) = \frac{1}{a + be^{-cx}} \tag{4}$$

$$\varepsilon(x) = d'(x) = \frac{bce^{-cx}}{(a + be^{-cx})^2} \tag{5}$$

where d is the accumulated displacement of each marker relative to the reference point; x is the distance from the wall face; a, b, and c are fitting constants; e is the base of the natural logarithm; and ε is the mobilized reinforcement tensile strain. A detailed description of the procedure for determining the reinforcement tensile strain can be found in the aforementioned references.

The advancement of the wetting front induced by rainfall and the drainage function of the sand cushions were visually observed using the fluorescent dyeing technique (Fig. 3c and d). Water-soluble fluorescent dye powders were distributed close to the transparent Plexiglas wall at a regular interval. The wall model was illuminated periodically by ultraviolet (UV) light using a UV lamp. The dissolved fluorescent dyes flowed with the water, displaying the seepage trace; this enabled direct visual observation of the flow line of the rainfall infiltration during the test. Compared with centrifuge tests, the 1-g model tests performed in this study have the advantage of allowing clearly observing the advancement of the wetting front and the direction of the seepage trace using the fluorescent dyeing technique. In addition, the 1-g model tests have a large wall model size that allows instrumentation, such as VWC sensors and PWP transducers, to be installed inside the wall. In contrast, the centrifuge tests have a relatively small wall model that only allows installing limited instrumentation to avoid disturbing the soil stress development in the centrifuge model.

3. Test results

This section details the test results of Test SM15 (the baseline case) and Test SM15+SC4. The results of other tests are summarized and compared together in next section. The time values in the test results are presented in the prototype scale.

3.1. Results of test SM15

Fig. 7 presents the wall deformation and shear strain field for Test SM15 with time. Fig. 8 displays the development of wall facing displacement for Test SM15 with time. Notably, the wall facing displacements measured in this study were additional displacements after the wall construction subject to rainfall. The line of $\Delta/H = 3\%$ plotted in

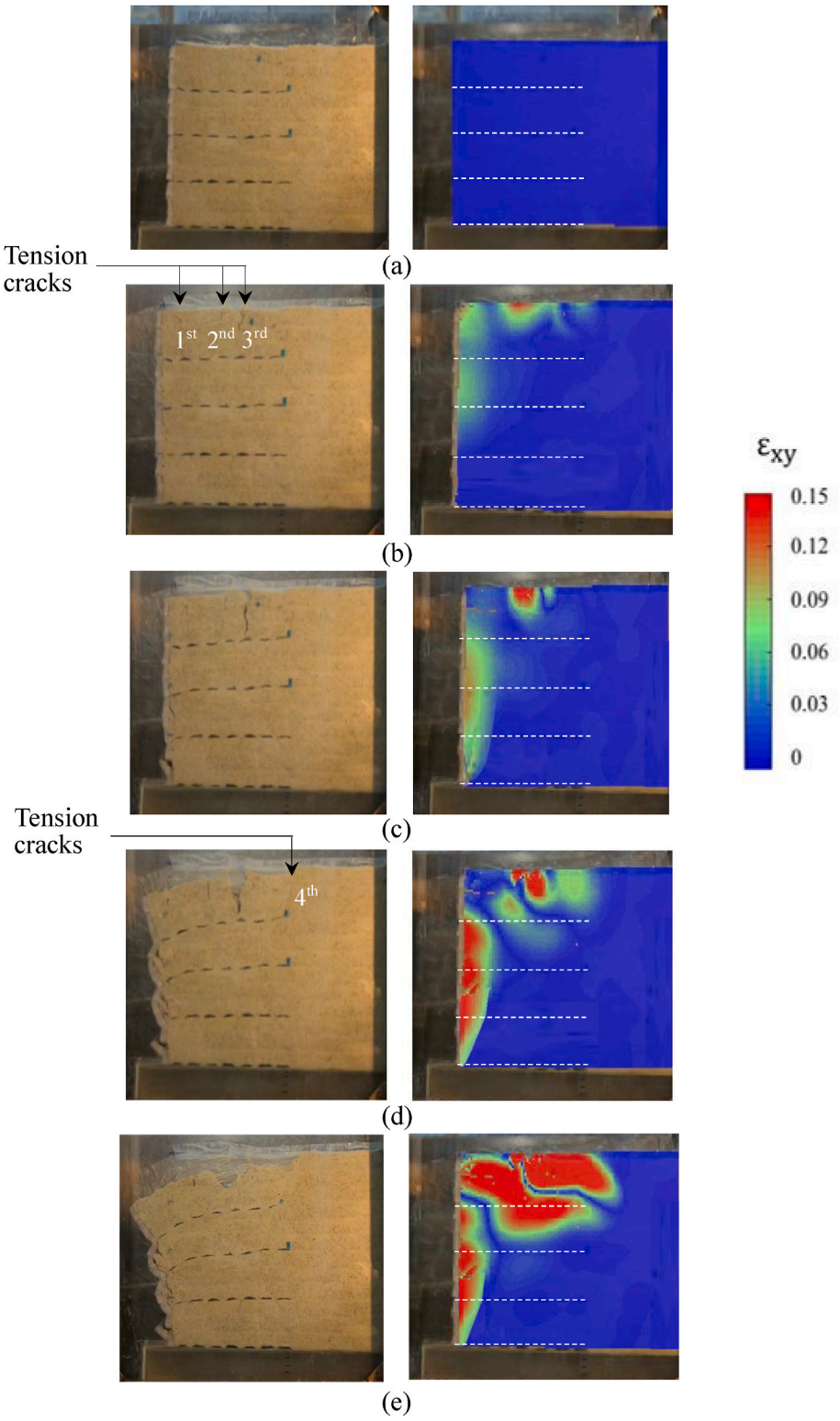

Fig. 7. Variation of wall deformation and shear strain field with time in Test SM15: t = (a) 0 min; (b) 265 min; (c) 275 min; (d) 325 min; (e) 375 min.

Fig. 8 represents a serviceability limit state of GRS walls according to the concept of the performance-based design. The Δ/H ranging from 1% to 3%, depending on $L//H$ and reinforcement extensibility, is generally used for estimating the wall facing displacements at the end of wall construction (EOC). The aforementioned Δ/H values were recommended in the design guidelines as performance criteria for evaluating the lateral facing displacement of GRS walls (Elias et al., 2001; WSDOT 2005; Berg et al., 2009; NCMA 2010; AASHTO 2012). Based on this performance criteria, the Δ/H = 3% was selected in this study as the serviceability limit state of GRS walls. The wall facing deformation was considered excessive if Δ/H > 3% because this condition exceeds the selected serviceability limit state.

At t = 265 min, the wall began to deform as the wetting front passed the midheight of the wall. Three tension cracks subsequently developed

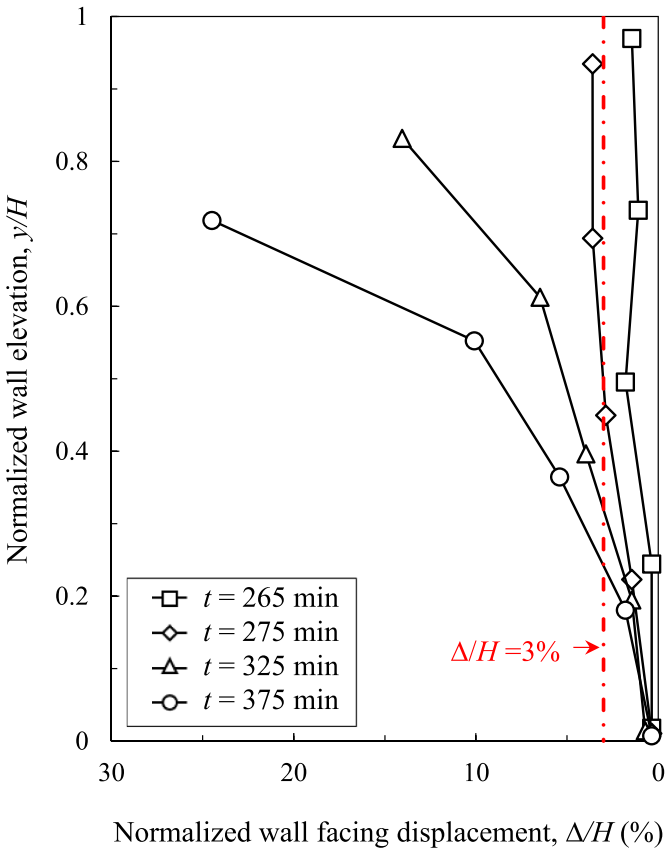

Fig. 8. Development of wall facing displacement with time in Test SM15.

at approximately 5, 20, and 25 cm from the wall crest (Fig. 7b). At t = 275 min, a third tension crack extended downward and the pullout of the wrap-around layer of the topmost reinforcement occurred (Fig. 7c). The wall deformation continued developing, and the normalized wall facing displacement increased to $\Delta/H > 3\%$ (Fig. 8). At t = 320 min, the wetting front reached the wall base, and the positive PWP values began to increase, indicating a rise in the phreatic surface level within the wall. At t = 325 min, the fourth tension crack developed immediately above the end of the topmost reinforcement layer. The pullout of the primary layer of the topmost reinforcement occurred, causing a remarkable subsidence at the boundary between the reinforced and retained zones (Fig. 7d). This subsidence enabled water ponding on the top of the wall, facilitating rainfall infiltration into the wall. The wall facing became cantilever-type displacement with a maximum displacement at the wall crest ($\Delta/H = 15\%$) that decreased with depth to zero displacement at the toe. At t = 375 min, the upper part of the wall collapsed due to excessive wall deformation of $\Delta/H \approx 25\%$ at the top (Figs. 7e and 8). The phreatic surface level increased to 13% of the wall height (i.e., $h/H = 13\%$) at the moment of wall failure.

The results of DIC analyses revealed that intense shear strain initially developed at the wall face and top of the wall (Fig. 7b). An intense shear strain progressed backward at the wall face and downward at the top as the rainfall proceeded. The intense shear strain at the wall face and at the top connected to form an active failure wedge at t = 275 min when $\Delta/H > 3\%$ (Fig. 7c). Subsequently, the intense shear strain at the upper part of the wall continued developing backward into the retained zone (Fig. 7d). Finally, a compound failure mode in which the failure surface partially cut through the reinforced zone and partially passed through the retained zone was observed when the wall collapsed (Fig. 7e). Similar compound failures have been reported as common failure modes for GRS structures with marginal backfill under heavy rainfall in several failure case histories (Liu et al., 2012; Yang et al., 2019a; Yoo and Jung 2006).

Fig. 9 displays the mobilization of reinforcement tensile strain with time. The shear strain contour at $\Delta/H \approx 3\%$ is also provided in Fig. 9 to indicate the initial failure surface. The reinforcement tensile strain gradually mobilized with time as the wall deformation continued developing. The locus of maximum tensile strain matches well with Rankine's failure surface, indicating the occurrence of active soil failure during the test. The maximum tensile strain value ($\varepsilon_{max} \approx 17\%$) developed at the topmost reinforcement layer in accordance with the excessive wall deformation at the top. Because of the use of the extensible reinforcements (i.e., the reinforcement failure strain was greater than the soil failure strain), the reinforcement did not break in the active soil state. The potential failure surface progressed backward until it reached the retained zone, forming a compound failure surface (the final failure surface in Fig. 9). A careful inspection of the retrieved reinforcement layers after the test revealed that the top two reinforcement layers were substantially distressed because the mobilized reinforcement strains at these two layers were close to the reinforcement failure strain value (Fig. 6).

3.2. Results of test SM15+SC4

Fig. 10 presents the wall deformation and shear strain field of Test SM15+SC4 with time. Fig. 11 presents the development of the wall facing displacement of Test SM15+SC4 with time. At t = 350 min, the wetting front reached the wall base, but no wall movement was observed. At t = 380 min, the wall started to deform, and a tension crack developed at approximately 20 cm from the wall crest (Fig. 10b). At t = 395 min, the second and third tension cracks developed at approximately 10 and 30 cm, respectively (Fig. 10c). At this time, pullout of the wrap-around layer of the topmost reinforcement occurred, forming a cantilever-type wall facing displacement, and Δ/H exceeded 3% at the top (Fig. 11). At t = 425 min (the end of the test), the displacement of the upper part of the wall above the topmost reinforcement layer reached Δ/H = 15% due to the pullout of the wrap-around layer of the topmost reinforcement. By contrast, the remainder of the wall remained stable (Fig. 10d and 11). The phreatic surface level had increased to 9.3% of the wall height (i.e., h/H = 9.3%) at the end of the test.

The results of the DIC analyses indicated that an intense shear strain initially developed at t = 380 min as the wall started to deform (Fig. 10b). The intense shear strain formed a clear active failure wedge at t = 395 min when $\Delta/H > 3\%$ (Fig. 10c). The final mode of wall failure was determined to be an excessive wall deformation due to the development of intense shear strain at the end of the test (Fig. 10d). Overall, the intense shear strain did not progress backward into the retained zone as those in Test SM15 did, demonstrating that the sand cushion can enhance the pullout resistance by improving the soil–reinforcement interface shear strength; hence, the sand cushion prevented the failure surface from progressing backward.

Fig. 12 displays the mobilization of reinforcement tensile strain with time. The maximum tensile strain value ($\varepsilon_{max} \approx 14\%$) occurred at the topmost reinforcement layer in accordance with the excessive wall deformation at the top. The failure surface depicted by the locus of maximum tensile strain was steeper than Rankine's failure surface. This difference in failure surfaces was likely because the inclination angle of Rankine's failure surface (i.e., $45^\circ + \varphi'/2$) was calculated using only the saturated friction angle of silty sand (the effect of the sand cushion was not considered in the calculation), resulting in an underestimate of the slope of the failure surface. These results also indicate the sand cushion improved the strength and deformation characteristics of the wall system, and thus generated a steep (or shallow) failure surface. The final failure surface, as indicated in Fig. 12, was associated with the cantilever-type wall deformation mode.

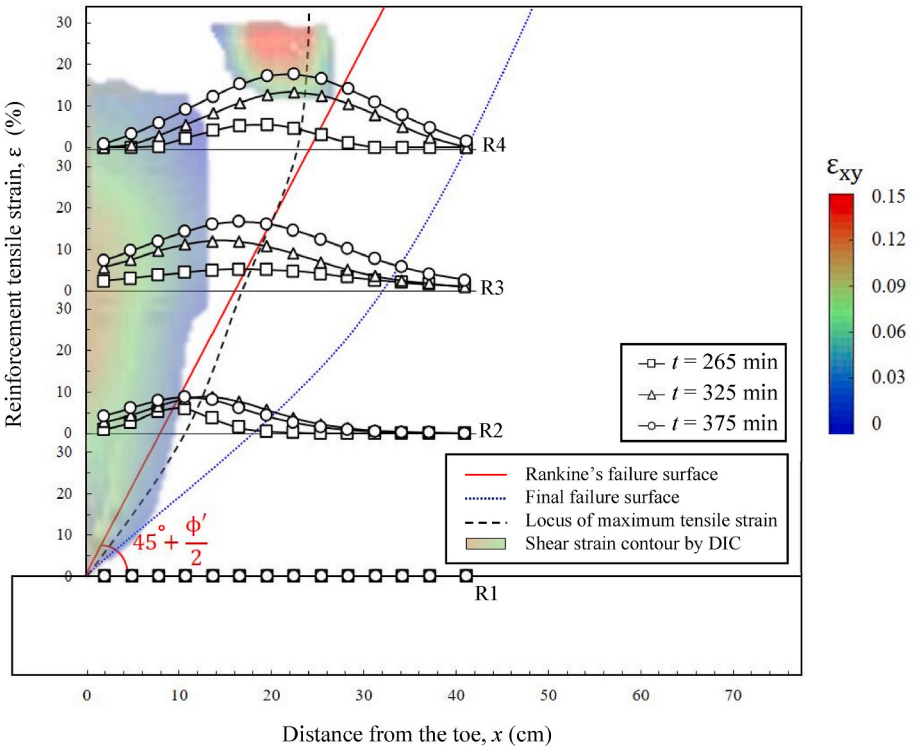

Fig. 9. Mobilization of reinforcement tensile strain with time and comparison of failure surfaces in Test SM15.

4. Overall comparison

This section presents an overall assessment of the performance of all wall models with various reinforcement spacings and sand cushion thicknesses. Table 6 summarizes the test results. The effectiveness of reinforcement spacing and sand cushion thickness in improving the drainage and stability of GRS walls is compared and discussed.

4.1. Rainfall infiltration and phreatic surface level

Fig. 13 displays a comparison of the advancement of the rainfall-induced wetting front with time for all tests. Based on the VWC readings at various depths, the advancement of the wetting front was determined at the time points when the soil VWC began to increase from the initial value. For the test group without sand cushions, the wetting front exhibited a similar propagation trend until t = 175 min. Subsequently, after the wall deformed, the rainfall infiltration pattern at the top of the wall as well as the seepage path inside the wall were changed, resulting in a change in the advancement of the wetting front. The time points at which the wetting front reached the wall base were t = 320, 295, and 290 min for Tests SM15, SM12, and SM10, respectively. The wall in Test SM20 collapsed before the wetting front reached the wall base. For the test group with sand cushions, the wetting front reached the wall base at t = 340, 350, and 425 min for Test SM15+SC2, SM15+SC4, and SM15+SC6, respectively. A comparison of the test groups reveals that the inclusion of sand cushion clearly delays the wetting front advancement. As the sand cushion thickness increased, the delay time of the wetting front advancement increased. This comparison results demonstrated the sand cushion could improve the drainage of the wall system and therefore delay the wetting front advancement.

Fig. 14 illustrates a comparison of the rise of the phreatic surface level with time for all tests. The red cross symbols in Fig. 14 indicate wall failures; thus, no observation data were obtained after these time points. The phreatic surface level began to rise soon after the wetting front arrived at the wall base. For the test group without sand cushions, the normalized phreatic surface levels at wall failure or at the end of test were h/H = 13%, 16.7%, and 18.7% for Tests SM15, SM12, and SM10, respectively. In Test SM20, the wall collapsed before the phreatic surface rose. For the test group with sand cushions, h/H = 9.5% and 9.3% for Test SM15+SC2, and SM15+SC4, respectively. No phreatic surface level rise was observed during Test SM15+SC6. The comparison results indicate the inclusion of sand cushions substantially lowered the phreatic surface level and therefore reduced the increase of PWP inside the wall.

Figs. 15 and 16 present the rainfall infiltration observed using the fluorescent dyeing technique for Tests SM15 and SM15+SC6, respectively. Overall, the observations of the wetting front advancement using the fluorescent dyeing technique agreed well with VWC measurements (Fig. 13). For Test SM15, the fluorescent dyes were initially distributed at regular intervals (blue illuminating color in Fig. 15a). As the rainfall proceeded, the fluorescent dyes dissolved and flowed in the water. A clear downward seepage trace, indicating the advancement of wetting front, in both the reinforced and retained zones can be observed (Fig. 15b). For SM15+SC6, Figs. 16a and b reveal that the wetting front reached the midheight, and bottom of the wall, respectively. Notably, the seepage trace within the sand cushions turned toward the wall facings, whereas the seepage trace between the sand cushions and in the retained zone remained vertically downward. This observation confirms the drainage function of sand cushions. Because the sand cushion has higher permeability than the backfill, the water flowed inside sand cushions and drained out through the sand cushions. Fig. 16b also reveals that the size of seepage trace in the reinforced zone at the lower half part of the wall was smaller than that in the retained zone at the same elevation. This result was attributed to the drainage function of sand cushions not only delaying rainfall infiltration but also reducing the downward rainfall infiltration. As a result, the seepage trace induced by rainfall infiltration in the reinforced zone at the lower half part of the wall was smaller than that in the retained zone.

4.2. Wall deformation and failure mode

Fig. 17 shows a comparison of the final wall facing displacement

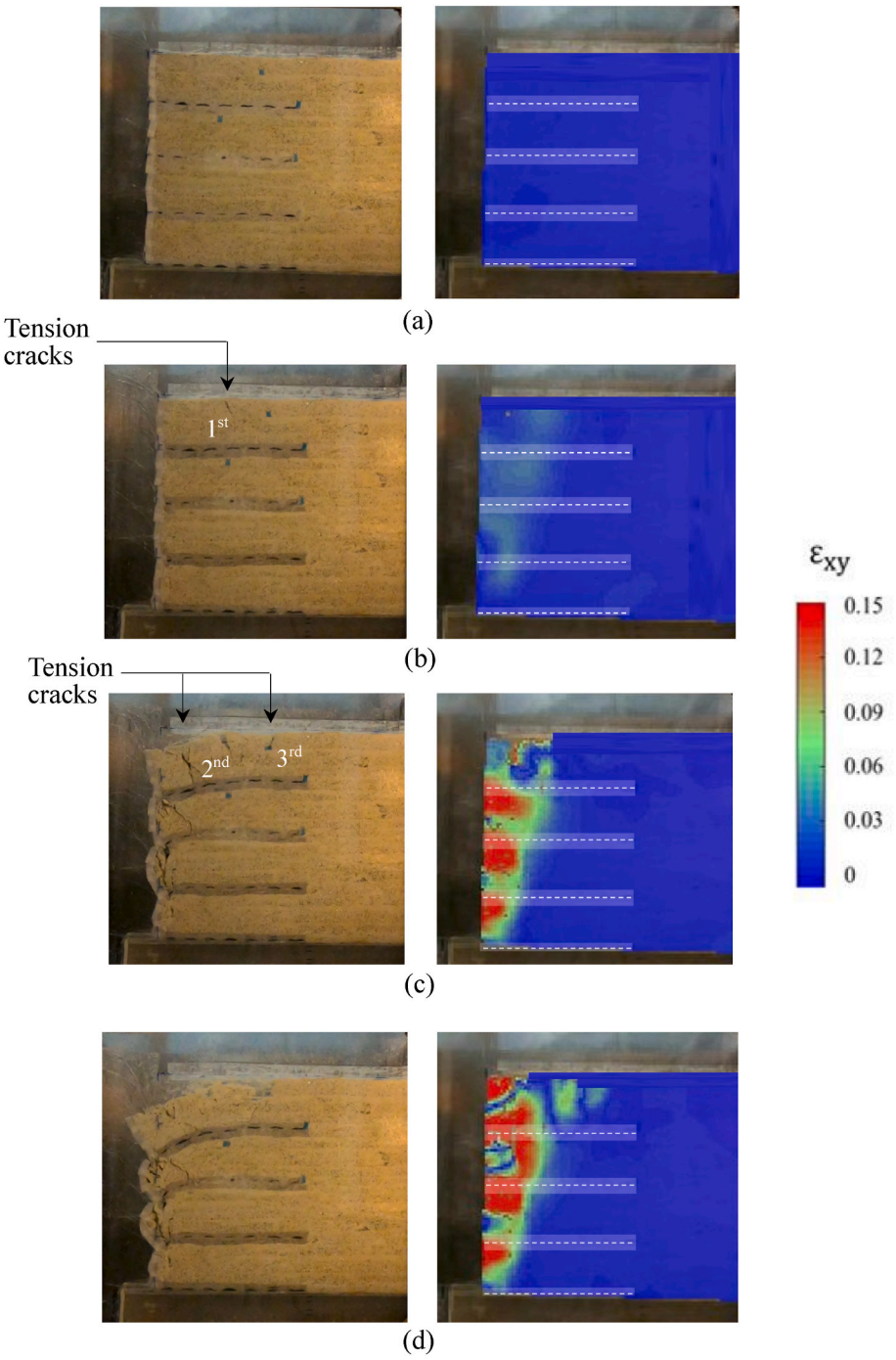

Fig. 10. Variation of wall deformation and shear strain field with time in Test SM15+SC4: t = (a) 0 min; (b) 380 min; (c) 395 min; (d) 425 min.

profiles for all tests. The maximum wall facing displacement occurred at the top of the wall, corresponding to a cantilever-type wall deformation pattern. Fig. 18 presents a comparison of the development of the maximum wall facing displacement with time for all tests. For the test group without sand cushions, the normalized maximum wall facing displacement at wall failure or the end of the test were $\Delta_{max}/H = 30.7\%$, 24.8%, and 4.5% for Tests SM20 and SM15, and SM12, respectively. No evident wall deformation was present in Test SM10. For the test group with sand cushions, $\Delta_{max}/H = 25.4\%$ and 19.1% for Tests SM15+SC2 and SM15+SC4, respectively. The wall for Test SM15+SC6 was stable with no displacement until the end of the test. A comparison of these results reveals that the wall deformation decreased as the reinforcement spacing decreased or the sand cushion thickness increased. A decrease in reinforcement spacing and an increase in sand cushion thickness could increase the global stiffness of the wall system and therefore restrain wall deformation.

Table 6 summarizes the failure modes. For the test group without sand cushions, a local failure (interlayer sliding) occurred in Test SM20; the part of wall above the topmost reinforcement slid off due to excessive wall deformation at the top. This local failure was attributed to the large reinforcement space. A compound failure was observed for Test SM15 as described in the previous section. Excessive deformation occurred in Test SM12 ($\Delta_{max}/H = 4.5\%$), but the wall did not collapse until the end of the test. For the test group with sand cushions, a compound failure was observed for Test SM15+SC2. The upper part of the wall collapsed due to excessive wall deformation. The final failure

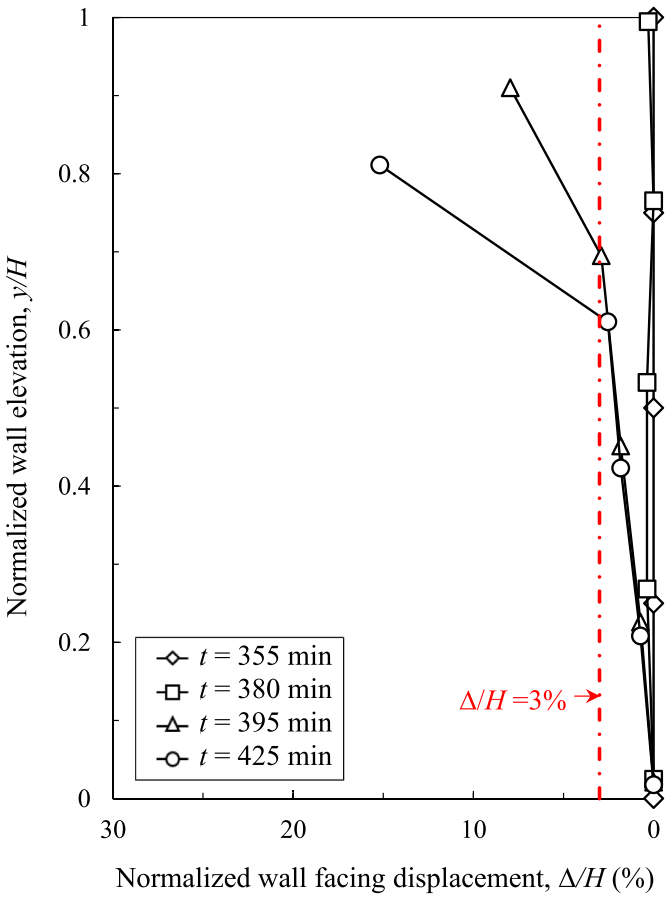

Fig. 11. Development of wall facing displacement with time in Test SM15+SC4.

surface was similar that observed in Test SM15. Excessive deformation at the upper part of the wall (Δ_{max}/H = 19.1%) was observed in Test SM15+SC4, as discussed in the previous section. Based on the test results, a decrease in reinforcement spacing or an increase in sand cushion thickness are both effective for improving wall stability and preventing wall collapse.

4.3. Reinforcement tensile strain mobilization

Fig. 19 presents a comparison of the final mobilized reinforcement tensile strain profile for all tests. Overall, the mobilized reinforcement tensile strain profile was correlated with the wall deformation pattern (Fig. 17). The mobilized reinforcement tensile strain had a maximum tensile strain value at the topmost reinforcement layer, and the tensile strain value decreased with depth. The firm foundation likely constrained both the soil movement and the reinforcement deformation at the base of wall, resulting in negligible tensile strains developing in the bottommost reinforcement layer (Yang et al., 2012). Moreover, the mobilization of reinforcement tensile strain at the lower part of the wall did not seem to be influenced by increases in the phreatic surface level (Fig. 14). As shown in Figs. 9 and 12, the reinforcement tensile strain at the lower part of the wall increases only slightly after the phreatic surface level rises.

Fig. 20 presents a comparison of the mobilization of ε_{max} values over time for all tests. The ε_{max} values for Tests SM20, SM15, and SM15+SC2 approximated or reached the reinforcement failure strain ($\varepsilon_f \approx 17\%$). Consequently, reinforcement could not provide further tensile resistance by mobilizing more tensile strain, and the upper part of the wall thus collapsed. The walls of Tests SM10 and SM15+SC4 experienced excessive deformation but did not collapse, and ε_{max} for these tests was 8.4% and 14%, respectively. The walls of Tests SM10 and SM15+SC6 did not develop any deformation; thus, no reinforcement strain was mobilized due to rainfall infiltration. The comparison indicates the mobilized reinforcement tensile strain decreased as the reinforcement spacing decreased or the sand cushion thickness increased. This trend was the same as that for wall deformation.

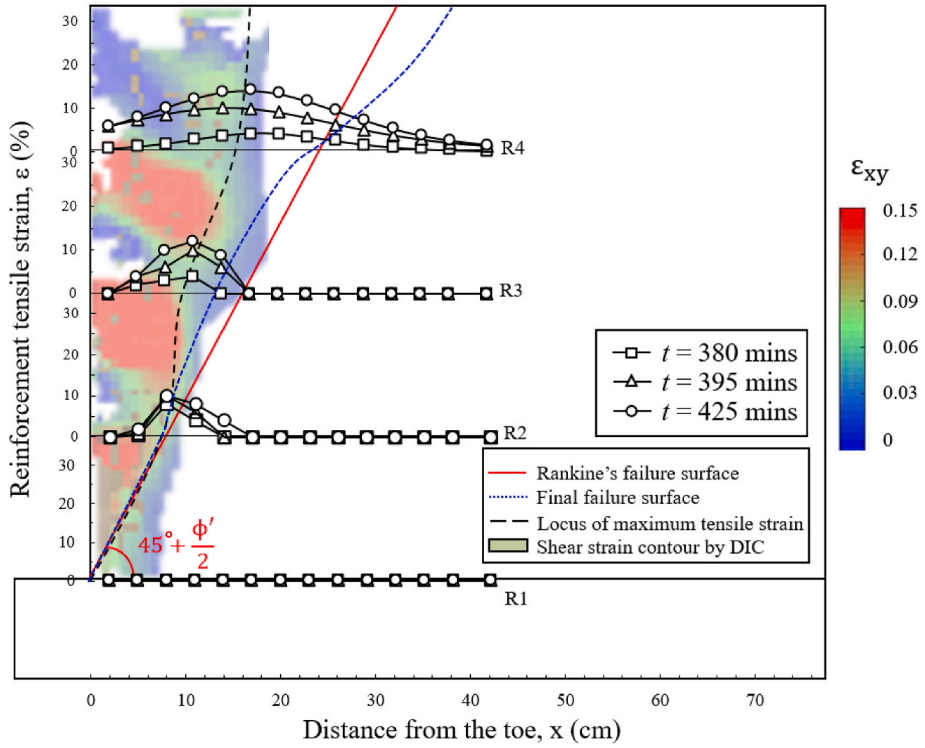

Fig. 12. Mobilization of reinforcement tensile strain with time and comparison of failure surfaces in Test SM15+SC4.

Table 6
Summary of the test results.

Test ID	Deformation and failure mode				Reinforcement	Phreatic level	
	Normalized maximum wall facing displacement, Δ_{max}/H (%)	Failure mode	Time when excessive wall deformation occurred (min)	Time when wall collapse occurred (min)	Maximum reinforcement tensile strain, ε_{max} (%)	Time when phreatic level rise (min)	h/H at the end of test (%)
SM 20	30.7	Local	215	280	17	–	0
SM 15	24.8	Compound	270	375	17	320	13
SM 12	4.5	Excessive deformation	380	–	8.6	295	16.7
SM 10	0	Stable	–	–	0	290	18.7
SM 15 + SC 2	25.4	Compound	340	415	16	340	9.5
SM 15 + SC 4	14.8	Excessive deformation	385	–	14	350	9.3
SM 15 + SC 6	0	Stable	–	–	0	–	0

Note: Δ_{max}/H was determined at wall failure or the end of the test. The wall excessive deformation was determined when $\Delta/H > 3\%$.

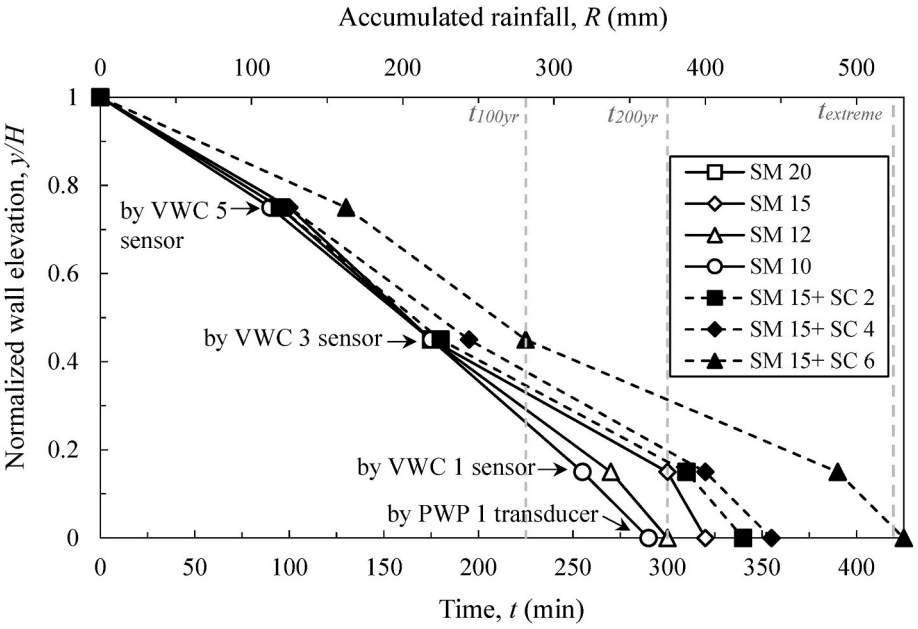

Fig. 13. Comparison of the advancement of wetting front with time.

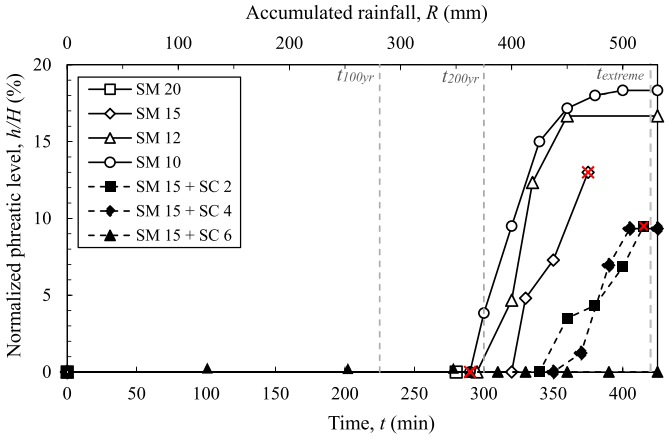

Fig. 14. Comparison of the rise of phreatic surface level with time.

5. Discussion of GRS wall design against rainfall

Two suggestions for designing GRS walls to withstand the effects of rainfall are discussed in this section.

5.1. Design considering site-specific hydrological conditions

The first suggestion regards the design of GRS walls considering site-specific hydrological conditions. The importance of evaluating the hydraulic response and stability of GRS walls by using realistic hydrological data has been highlighted by Yang et al. (2019b) and Nunes et al. (2022). The resilience of GRS walls with marginal backfill during extreme precipitation events was numerically assessed by Vahedifard et al. (2017) using hydrological data from the Seattle region. The results of their study indicated that extreme precipitation events can greatly affect the performance of GRS walls. In this study, the performance of GRS walls was evaluated under three rainfall scenarios: 100- and 200-year rainfall events and future extreme weather events that may occur due to long-term climate change. The corresponding rainfall durations on the prototype scale in the three selected rainfall scenarios were t_{100yr} = 225 min, t_{200yr} = 300 min, and $t_{extreme}$ = 420 min, respectively. The t_{100yr} and t_{200yr} values were the rainfall durations of the 100- and 200-year return periods determined from the rainfall

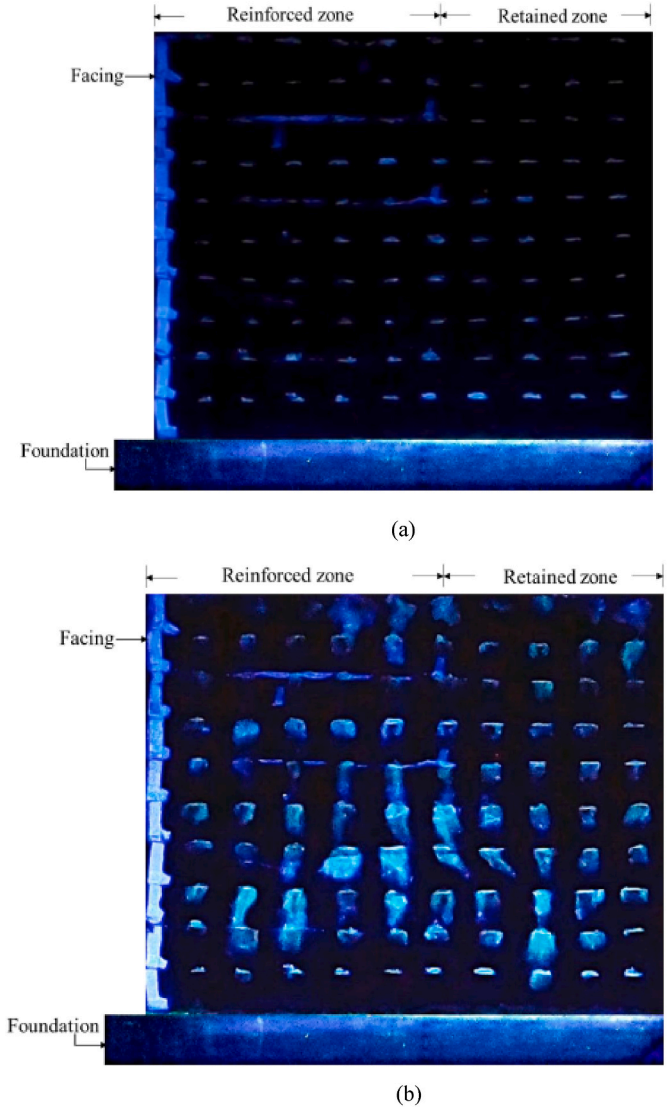

Fig. 15. Observation of rainfall infiltration using fluorescent dyeing technique: Test SM12 (a) $t = 0$ min; (b) $t = 320$ min.

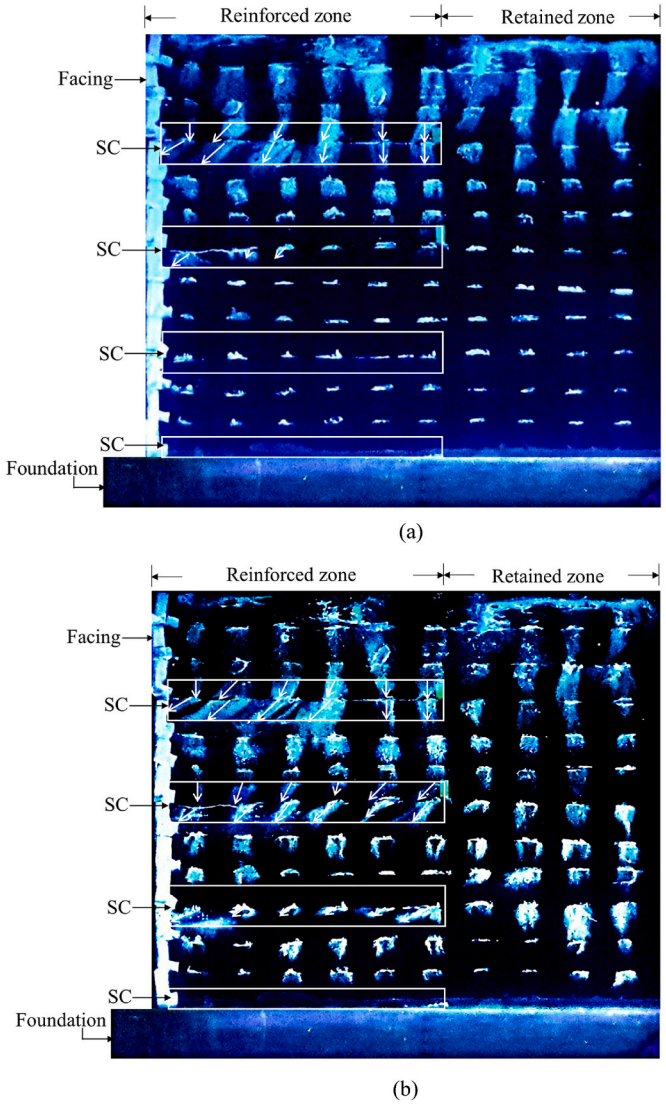

Fig. 16. Observation of rainfall infiltration using fluorescent dyeing technique: SM15 + SC6 (a) $t = 280$ min; (b) $t = 425$ min.

intensity–duration–frequency (I–D–F) curves for the Taipei region using hydrological data provided by the Taiwan Central Weather Bureau. The total accumulated rainfall for t_{100yr} and t_{200yr} were 281 and 375 mm, respectively, on the prototype scale, representing "extremely heavy rain" and "torrential rain" conditions as defined by the Taiwan Central Weather Bureau. The $t_{extreme}$ was calculated according to the information provided by the Taiwan Climate Change Projection and Information Platform (TCCIP), which states that the average annual rainfall in the Taipei region will increase by ≈ 1.4 times over the next 100 years. The total accumulated rainfall for $t_{extreme}$ reaches 525 mm on the prototype scale; this is classified as "extremely torrential rain" by the Taiwan Central Weather Bureau.

Table 7 lists the wall performance under the three rainfall scenarios for all tests. In Table 7, wall failure was defined as either wall collapse or as excessive wall deformation with $\Delta/H > 3\%$. For a 100-year rainfall event, the wall in Test SM20 developed excessive deformation ($\Delta_{max}/H = 5.3\%$); the walls in other tests remained stable. For the 200-year rainfall event, the wall of Test SM20 collapsed, and the wall of Test SM15 developed excessive deformation ($\Delta_{max}/H = 10.8\%$), whereas the walls in other tests still performed satisfactorily. Under the future extreme weather event, only the walls of Tests SM 10 and SM15+SC6 were stable without displacement; the other walls failed. The GRS walls in the various tests performed differently in the three selected rainfall scenarios because the performance of GRS structures subjected to rainfall involves complex interactions and mutual influence among the hydrological, geotechnical, and geosynthetic parameters. Thus, the site-specific potential rainfall should be taken into account when designing GRS walls to resist rainfall, particularly if marginal soil is used as backfill. Robust design methods that couple both hydrological, geotechnical, and geosynthetic parameters must be adopted to obtain an optimal design for rainfall-resistant GRS structures.

5.2. Stability analyses of GRS walls

The second suggestion regards stability analyses of GRS walls. Table 2 lists the calculated FS values for internal stability against reinforcement breakage and pullout. Although the FSs are larger than 1.0 for all tests; wall failure still occurred under various rainfall scenarios. This was attributed that the compound failure, rather than the internal failure used to determine FSs, was the predominant failure mode as observed in the tests. Because of the use of the extensible reinforcements, the reinforcement did not break in the active soil state. The potential failure surface progressed backward until it reached the retained zone, resulting in the collapse of the GRS wall in a compound

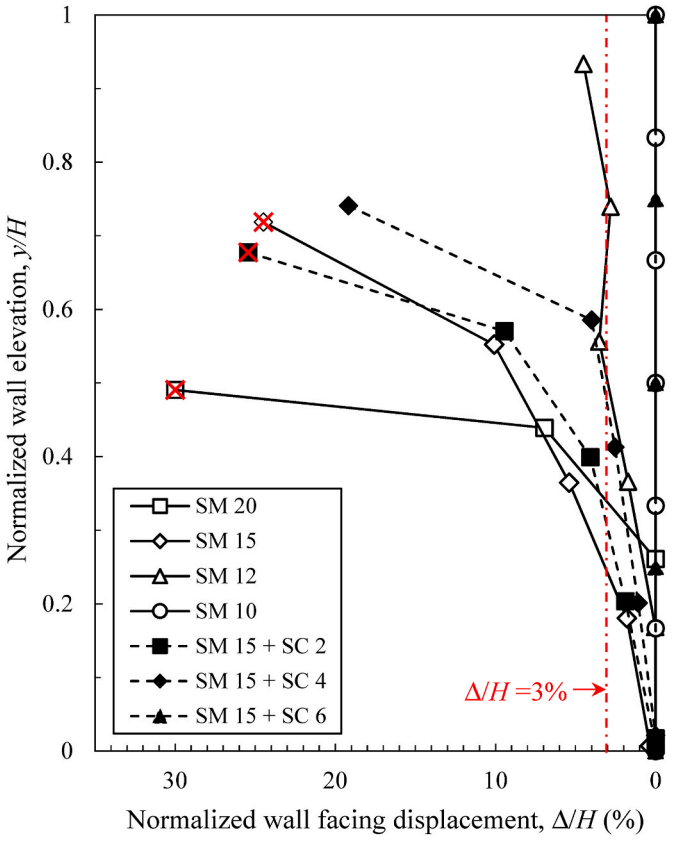

Fig. 17. Comparison of the final wall facing displacement profile.

failure mode. However, the compound failure mode is often overlooked in the practical design; this has resulted in failures of GRS structures, as reported in several failure case histories (Liu et al., 2012; Yang et al., 2019a; Yoo and Jung 2006). The above discussion highlights the importance of the evaluation of the wall stability against compound failure using limit equilibrium analyses. Moreover, the tests revealed that walls could develop excessive deformation even though they did not completely collapse. For the design of GRS walls with marginal backfill, wall deformation cannot be simply presumed to be within tolerable limits when the FS requirements for internal or external failure have been satisfied. Deformation response analyses using advanced numerical methods (i.e., finite element method) are recommended for evaluating the anticipated displacement of the GRS structures to guarantee that the wall performance is within the serviceability limit upon rainfall.

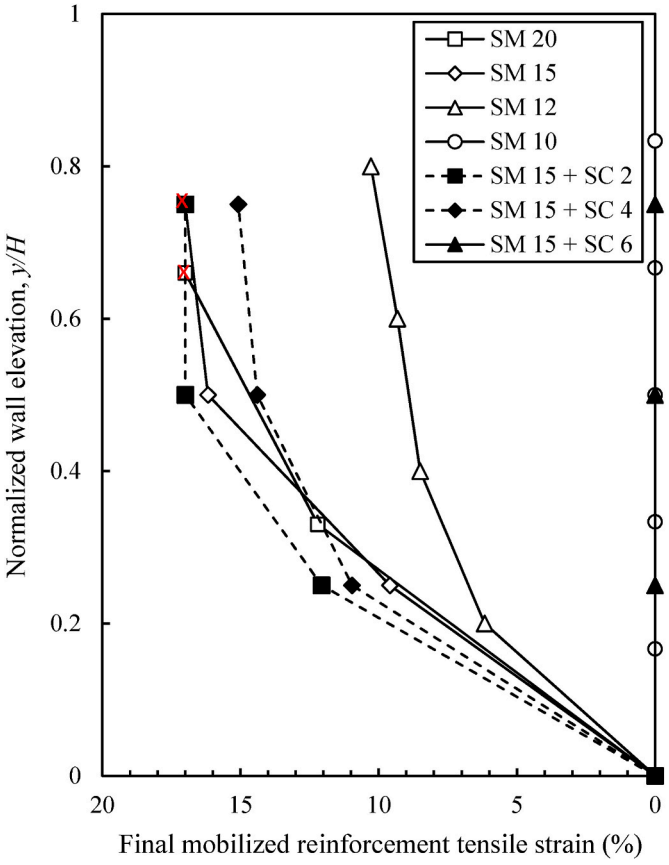

Fig. 19. Comparison of the final mobilized reinforcement tensile strain profile.

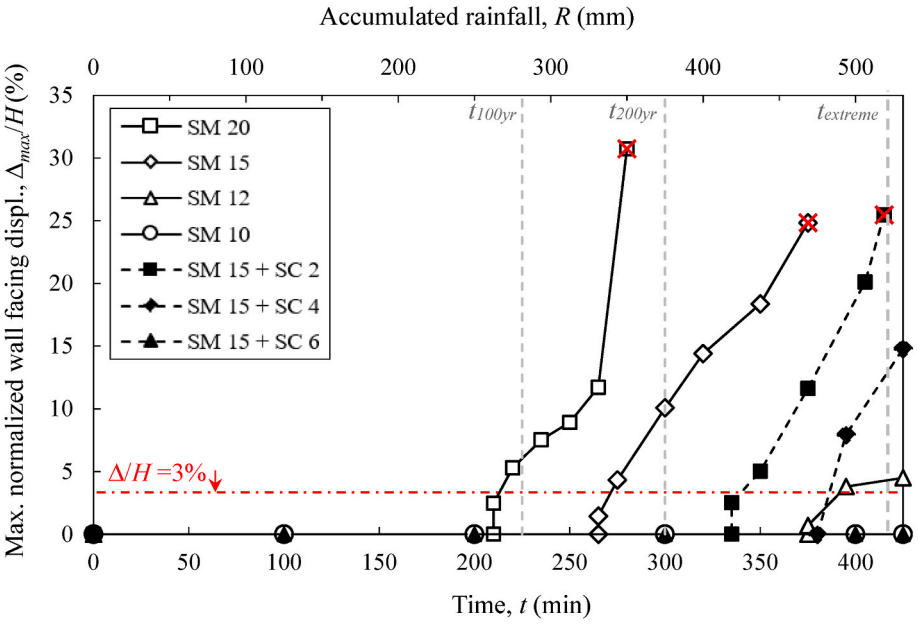

Fig. 18. Comparison of the development of maximum wall facing displacement with time.

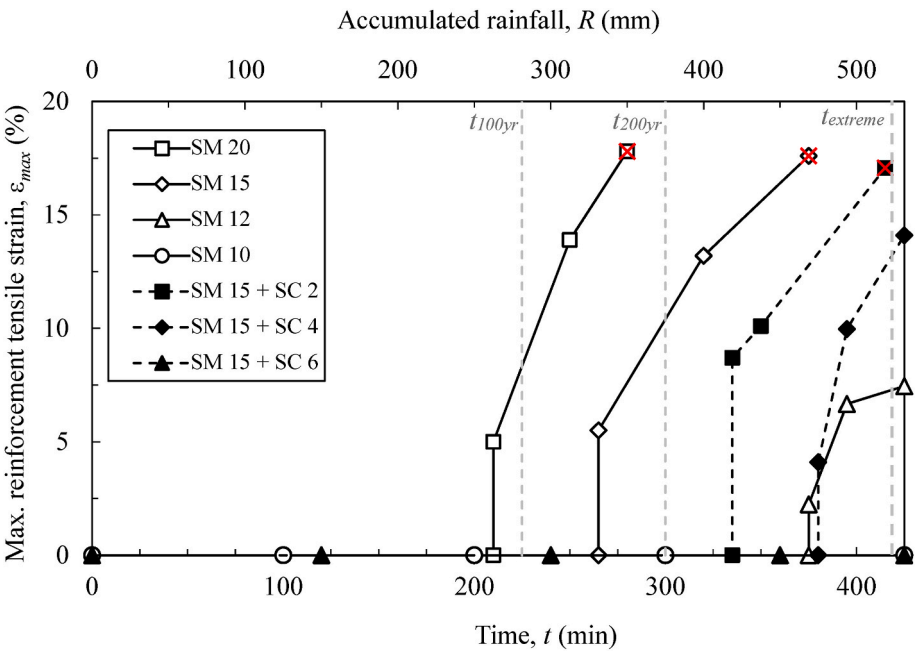

Fig. 20. Comparison of the mobilization of maximum reinforcement tensile strain with time.

Table 7
Wall performance under the three rainfall scenarios.

Rainfall scenario	Rainfall duration (min)	Accumulative rainfall (mm)	Wall failure
100-year rainfall event	225	281	SM20 ($\Delta_{max}/H = 5.3\%$)
200-year rainfall event	300	375	SM20 (Collapse) SM15 ($\Delta_{max}/H = 10.8\%$)
Future extreme weather event	420	525	SM20 (Collapse) SM15 (Collapse) SM 12 ($\Delta_{max}/H = 4\%$) SM15+SC 2 (Collapse) SM15+SC4 ($\Delta_{max}/H = 12\%$)

Note: the wall failure was determined including either wall collapse or excessive wall deformation when $\Delta/H > 3\%$.

6. Conclusions

A series of model tests on GRS walls with marginal backfill subjected to rainfall infiltration were conducted to investigate the performance of GRS walls during rainfall. The effects of reinforcement spacing and sand cushion thickness on the wall performance were evaluated quantitatively. The following conclusion were drawn according to the experimental results:

1. For Test SM15 (the baseline case), the wall began to deform when the wetting front passed the midheight of the wall. Several tension cracks developed at the top of the wall. As rainfall proceeded, the wall continued deforming, causing the potential failure surface to gradually move backward. When the potential failure surface moved beyond the reinforced zone, the pullout of the topmost reinforcement layers occurred, resulting in the collapse of the GRS wall in a compound failure mode.
2. The test results demonstrate that placing sand cushions in marginal soil yields the following three advantages. First, the sand cushion can improve the pullout resistance by increasing the shear strength of the soil–reinforcement interface, preventing the occurrence of the compound failure. Second, the sand cushion can improve the strength and deformation characteristics of the wall system; thus, restrains the wall deformation and reduces the mobilized reinforcement tensile strain required for equilibrium. Third, the sand cushion can improve the drainage of the wall system, delaying the advancement of the wetting front and reducing the accumulation of PWP inside the wall.
3. The test results for the various walls suggest that the decrease in reinforcement spacing and increase in sand cushion thickness could effectively reduce wall deformation and increase wall stability.
4. This study demonstrated that the fluorescent dyeing technique was useful for visually observing the advancement of the wetting front and the direction of the seepage trace.
5. Based on the test tests, the GRS walls of various tests performed differently in the three selected rainfall scenarios, suggesting that rain-resistant GRS walls, particularly those in which marginal soil is used as backfill, should be designed in accordance with the site-specific potential rainfall.
6. The test results revealed that wall failures feature both compound failure and excessive wall deformation. Stability analyses should be conducted to evaluate wall displacement and compound failure mode to ensure that the wall performs within serviceable limits upon rainfall.

In this study, the performance of GRS walls with only one type of marginal soil was evaluated. Future studies are suggested to investigate the effects of marginal soil parameters (i.e., fines content, PI, and hydraulic conductivity) on the performance of GRS walls. Besides, the effects of reinforcement spacing and sand cushion thickness could work in

tandem in influencing the performance of GRS walls. The combined effect of these two parameters requires further investigation for an optimal design.

Data availability

Data will be made available on request.

Acknowledgements

The financial support for this research was from the Ministry of Science and Technology of Taiwan under grant no. MOST 107-2628-E002-003-MY3. The second author would like to acknowledge the Ph.D. scholarship for his study provided by the Sinotech Foundation for Research & Development of Engineering Sciences &Technologies. These financial supports are gratefully acknowledged.

Notation List

Basic SI units are given in parentheses

a, b, c	fitting constants (dimensionless)
c'	cohesion (kN/m^2)
D_{50}	mean particle size (m)
D_{max}	maximum particle size (m)
D_r	relative density (dimensionless)
d	accumulated reinforcement displacement (m)
E_τ	efficiency factor (dimensionless)
F	fines content (%)
G_s	specific gravity (dimensionless)
g	gravitational acceleration (m/s^2)
H	wall height (m)
h	phreatic surface level (m)
h/H	normalized phreatic surface level (%)
I	rainfall intensity (m/s)
$J_{2\%}$	secant stiffness at 2% strain (kN/m)
J	stiffness at failure (kN/m)
K_a	active earth pressure coefficient (dimensionless)
k	Saturated hydraulic conductivity (m/s)
L	reinforcement length (m)
l	seepage length (m)
N	scaling factor (dimensionless)
R	accumulated rainfall (mm)
t	time/rainfall duration (s)
t_{100yr}	duration of 100-year rainfall event (s)
t_{200yr}	duration of 200-year rainfall event (s)
$t_{extreme}$	duration of future extreme weather event (s)
U_c	rainfall uniformity (%)
S_v	vertical spacing (m)
s_g	aperture size (m)
T	tensile force (kN/m)
T_{ult}	ultimate tensile strength (kN/m)
x	distance from the toe (m)
y/H	normalized wall elevation (dimensionless)
β	wall inclination angle (°)
Δ	wall facing displacement (m)
Δ_{max}	maximum wall facing displacement (m)
Δ_{max}/H	maximum normalized wall facing displacement (%)
δ	interface friction angle (°)
ε	tensile strain (%)
ε_{xy}	shear strain (%)
ε_f	failure strain (%)
ε_{max}	maximum tensile strain (%)
φ'	friction angle (°)
γ	soil unit weight (kN/m^3)
$\gamma_{d,max}$	maximum dry unit weight (kN/m^3)
$\gamma_{d,min}$	minimum dry unit weight (kN/m^3)
ρ	mass density of the fluid (kg/m^3)
μ	viscosity of the fluid (kN·s/m^2)
ω_{opt}	optimum water content (%)

Abbreviations

AASHTO	American Association of State Highway and Transportation
ASTM	American Society for Testing and Materials
DIA	digital image analysis
DIC	digital image correlation
FS	factor of safety
GRS	geosynthetic-reinforced soil
LL	liquid limit
PE	polyethylene
PET	polyester
PI	plasticity index
PL	plastic limit
PWP	porewater pressure
SC	sand cushion
SM	silty sand
TCCIP	Taiwan Climate Change Projection and Information Platform
USCS	unified soil classification system
UV	ultraviolet
VWC	volumetric water content

References

Aashto, 2002. Standard Specifications for Highway Bridges. American Association of State Highway and Transportation Officials, Washington, DC, with interims.

Abdi, M.R., Zandieh, A.R., 2014. Experimental and numerical analysis of large scale pull out tests conducted on clays reinforced with geogrids encapsulated with coarse material. Geotext. Geomembranes 42 (5), 494–504.

Abdi, M.R., Sadrnejad, A., Arjomand, M.A., 2009. Strength enhancement of clay by encapsulating geogrids in thin layers of sand. Geotext. Geomembranes 27 (6), 447–455.

Albino, U.R., Portelinha, F.H.M., Futai, M.M., 2020. Numerical simulation of a geotextile soil wall considering soil-atmosphere interaction. Geosynth. Int. 27 (4), 394–413.

Allen, T.M., Bathurst, R.J., 2019. Geosynthetic reinforcement stiffness characterization for MSE wall design. Geosynth. Int. 26 (6), 592–610.

ASTM D 698. Standard Test Methods for Laboratory Compaction Characteristics of Soil Using Standard Effort (12 400 Ft-Lbf/ft3, 600 kN- M/m3), ASTM Standards, ASTM International, West Coshohocken, Pnnsylvania, USA.

ASTM-D2434 Standard Test Methods for Permeability of Granular Soils (Constant Head). ASTM Standards, ASTM International, West Coshohocken, Pnnsylvania, USA.

ASTM-D3080. Standard Test Method for Direct Shear Test of Soils under Consolidated Drained Conditions. ASTM Standards, ASTM International, West Coshohocken, Pnnsylvania, USA.

ASTM-D4253. Standard Test Methods for Maximum Index Density and Unit Weight of Soils Using a Vibratory Table. ASTM Standards, ASTM International, West Coshohocken, Pnnsylvania, USA.

ASTM-D4254. Standard Test Methods for Maximum Index Density and Unit Weight of Soils and Calculation of Relative Density. ASTM Standards, ASTM International, West Coshohocken, Pnnsylvania, USA.

ASTM-D4595. Standard Test Method for Tensile Properties of Geotextiles by the Wide-Width Strip Method. ASTM Standards, ASTM International, West Coshohocken, Pnnsylvania, USA.

ASTM-D5084. Standard Test Methods for Measurement of Hydraulic Conductivity of Saturated Porous Materials Using a Flexible Wall Permeameter. ASTM Standards, ASTM International, West Coshohocken, Pnnsylvania, USA.

Baker, W.E., Westine, P.S., Dodge, F.T., 1991. Similarity Methods in Engineering Dynamics - Theory and Practice of Scale Modeling. Elsevier Science Publishers B.V., The Netherlands.

Balakrishnan, S., Viswanadham, B.V.S., 2016. Performance evaluation of geogrid reinforced soil walls with marginal backfills through centrifuge model tests. Geotext. Geomembranes 44 (1), 95–108.

Balakrishnan, S., Viswanadham, B., 2019. Centrifuge model studies on the performance of soil walls reinforced with sand-cushioned geogrid layers. Geotext. Geomembranes 47 (6), 803–814.

Bathurst, R.R., Naftchali, F.M., 2021. Geosynthetic reinforcement stiffness for analytical and numerical modelling of reinforced soil structures. Geotext. Geomembranes 49 (4), 921–940.

Berg, R.R., Christopher, B.R., Samtani, N., 2009. Design of Mechanically Stabilized Earth Walls. In: FHWA-NHI-10-024, vols. I and II (Washington, DC, USA).

Bhattacherjee, D., Viswanadham, B.V.S., 2015. Numerical studies on the performance of hybrid-geosynthetic-reinforced soil slopes subjected to rainfall. Geosynth. Int. 22 (6), 411–427.

Bhattacherjee, D., Viswanadham, B.V.S., 2019. Centrifuge model studies on performance of hybrid geosynthetic–reinforced slopes with poorly draining soil subjected to rainfall. J. Geotech. Geoenviron. Eng. 145 (12), 04019108.

Blaber, J., Adair, B., Antoniou, A., 2015. Ncorr: open-source 2D digital image correlation Matlab software. Exp. Mech. 55 (6), 1105–1122.
Brandl, H., 2011. Geosynthetics applications for the mitigation of natural disasters and for environmental protection. Geosynth. Int. 18 (6), 340–390.
Buckingham, E., 1914. On physically similar systems: illustrations of the use of dimensional equations. Phys. Rev. 4 (4), 345–376.
Chen, J.F., Yu, S.B., 2011. Centrifugal and numerical modeling of a reinforced lime-stabilized soil embankment on soft clay with wick drains. Int. J. GeoMech. 11 (3), 167–173.
Chinkulkijniwat, A., Horpibulsuk, S., Bui Van, D., Udomchai, A., Goodary, R., Arulrajah, A., 2016. Influential factors affecting drainage design considerations for mechanical stabilised earth walls using geocomposites. Geosynth. Int. 24 (3), 1–18.
Elias, V., Christopher, B.R., Berg, R., 2001. Mechanically Stabilized Earth Walls and Reinforced Soil Slopes Design and Construction Guidelines. National Highway Institute, Federal Highway Administration, Washington, D.C.
Fowze, J.S.M., Bergado, D.T., Soealump, S., Voottipreux, P., Dechasakulsom, M., 2012. Rain-triggered landslide hazards and mitigation measures in Thailand: from research to practice. Geotext. Geomembranes 30, 50–64.
Fox, P.J., 2022. Analytical solutions for internal stability of a geosynthetic-reinforced soil retaining wall at the limit state. J. Geotech. Geoenviron. Eng. 148 (10), 04022076.
Garcia, E.F., Gallage, C.P.K., Uchimura, T., 2007. Function of permeable geosynthetics in unsaturated embankments subjected to rainfall infiltration. Geosynth. Int. 14 (2), 89–99.
Guo, W., Wang, X., He, C., Jiang, L., Long, Y., Guo, Z., Yan, Z., Zhao, L., Lin, Y., 2022. Seismic performance of near-fault geosynthetic-reinforced pile-supported embankment. Geosynth. Int. https://doi.org/10.1680/jgein.21.00105.
Hadded, A., Shafabakhsh, G., 2008. Failure of segmental retaining walls due to the insufficiency of backfill permeability. Geosynthetics in Civil and Environmental Engineering 852–856.
Hossain, M.S., Kibria, G., Khan, M.S., Hossain, J., Taufiq, T., 2012. Effects of backfill soil on excessive movement of MSE wall. J. Perform. Constr. Facil. 26 (6), 793–802.
Iryo, T., Rowe, R.K., 2005. Infiltration into an embankment reinforced by nonwoven geotextiles. Can. Geotech. J. 42 (4), 1145–1159.
Jayanandan, M., Viswanadham, B.V.S., 2019. Geogrid reinforced soil walls with marginal backfills subjected to rainfall: numerical study. Indian Geotech. J. 50 (2), 238–251.
Koerner, R.M., Koerner, G.R., 2011. The importance of drainage control for geosynthetic reinforced mechanically stabilized earth walls. Journal of GeoEngineering 6 (1), 3–13.
Koerner, R.M., Koerner, G.R., 2013. A database, statistics and recommendations regarding 171 failed geosynthetic reinforced mechanically stabilized earth (MSE) walls. Geotext. Geomembranes 40, 20–27.
Koerner, R.M., Koerner, G.R., 2018. An extended data base and recommendations regarding 320 failed geosynthetic reinforced mechanically stabilized earth (MSE) walls. Geotext. Geomembranes 46 (6), 904–912.
Koseki, Shibuya, S., 2014. Mitigation of disasters by earthquakes, tsunamis, and rains by means of Geosynthetic-reinforced soil retaining walls and embankments. Transportation Infrastructure Geotechnology 2 (1), 231–261.
Kuwano, J., Miyata, Y., Koseki, J., 2012. Performance of reinforced soil walls during the 2011 Tohoku earthquake. Geosynth. Int. 21 (3), 179–196.
Lambert, S., Bourrier, F., 2013. Desing of rockfall protection embankments: a review. Eng. Geol. 154, 77–88.
Leonards, G.A., Frost, J.D., Bray, J.D., 1994. Collapse of geogrid-reinforced retaining structure. J. Perform. Constr. Facil. 8 (4), 274–292.
Lin, C.-Y., Yang, K.-H., 2014. Experimental study on measures for improving the drainage efficiency of low-permeability and low-plasticity silt with nonwoven geotextile drains. Journal of the Chinese Institute of Civil and Hydraulic Engineering 26 (2), 71–82 (In Chinese).
Liu, C.-N., Yang, K.-H., Ho, Y.-H., Chang, C.-M., 2012. Lessons learned from three failures on a high steep geogrid-reinforced slope. Geotext. Geomembranes 34, 131–143.
Liu, C.-N., Yang, K.-H., Nguyen, M.D., 2014. Behavior of geogrid-reinforced sand and effect of reinforcement anchorage under large-scale plane strain compression. Geotext. Geomembranes 42, 479–493.
Mamaghanian, J., Viswanadham, B., Razeghi, H., 2019. Centrifuge model studies on geocomposite reinforced soil walls subjected to seepage. Geosynth. Int. 26 (4), 371–387.
Mitchell, J.K., Zornberg, J.G., 1995. Reinforced soil structures with poorly draining backfills part II: case histories and applications. Geosynth. Int. 2 (1), 265–307.
Miyata, Y., Shinoda, M., 2016. A case study of damages of geogrid reinforced soil walls triggered by rainfall. *The 6th Asian Regional Conference on Geosynthetics, Geosynthetics Asia 2016* (Deli, India).
Mohammad, S.A., Parastoo, N.M., 2017. Effect of geogrid aperture size and soil particle size on geogrid-soil interaction under pullout loading. Journal of Textiles and Polymers 5 (1), 25–30.
Muir Wood, D., 2004. Geotechnical Modeling. Taylor and Francis.
NCMA, 2010. In: Bernardi, M. (Ed.), *Design Manual For Segmental Retaining Walls*, National Concrete Masonry Association. Herndon, Virginia, USA.
Nunes, G.B., Portelinha, F.H.M., Futai, M.M., Yoo, C., 2022. Numerical study of climate conditions on stailbty of geocomposite and geogrd reinfroced soil walls. Geotext. Geomembranes 50 (4), 807–824.
Portelinha, F.H.M., Zornberg, J.G., 2017. Effect of infiltration on the performance of an unsaturated geotextile-reinforced soil wall. Geotext. Geomembranes 45 (3), 211–226.
Portelinha, F.H.M., Bueno, B.S., Zornberg, J.G., 2013. Performance of nonwoven geotextile-reinforced walls under wetting conditions: laboratory and field investigations. Geosynth. Int. 20 (2), 90–104.
Portelinha, F., Santos, M., Futai, M., 2021. A laboratory evaluation of reinforcement loads induced by rainfall infiltration in geosynthetic mechanically stabilized earth walls. Geotext. Geomembranes 49 (5), 1427–1439.
Raisinghani, D.V., Viswanadham, B.V.S., 2010. Evaluation of permeability characteristics of a geosynthetic-reinforced soil through laboratory tests. Geotext. Geomembranes 28 (6), 579–588.
Raisinghani, D.V., Viswanadham, B.V.S., 2011. Centrifuge model study on low permeable slope reinforced by hybrid geosynthetics. Geotext. Geomembranes 29 (6), 567–580.
Razeghi, H.R., Viswanadham, B., Mamaghanian, J., 2019. Centrifuge and numerical model studies on the behaviour of geogrid reinforced soil walls with marginal backfills with and without geocomposite layers. Geotext. Geomembranes 47 (5), 671–684.
Recio-Molina, J., Yasuhara, K., 2005. Stability of modified geotextile wrap around revetments for coastal protection. Geosynth. Int. 12 (5), 260–268.
Ren, F., Huang, Q., Chen, J., 2022. Centrifuge modeling of geosynthetic-reinforced soil retaining walls subjected to the combined effect of earthquakes and rainfall. Geotext. Geomembranes 50 (3), 470–479.
Saran, R., Viswanadham, B., 2018. Centrifuge model tests on the use of geosynthetic layer as an internal drain in levees. Geotext. Geomembranes 46 (3), 257–276.
Scarborough, J.A., 2005. A tale of two walls: case histories of failed MSE walls. Proceedings of Geo-Frontiers 2751–2762.
Shibuya, S., Kawaguchi, T., Chae, J., 2007. Failure of reinforced earth as attacked by typhoon No. 23 in 2004. Soils Found. 47 (1), 153–160.
Shibuya, S., Hur, J., Jung, M., Kim, B., 2011. Case study on rainfall-induced behavior of unsaturated soils in natural slopes and reinforced-earth walls. International Symposium on Deformation Characteristics of Geomaterials 141–180.
Thuo, J.N., Yang, K.H., Huang, C.C., 2015. Infiltration into unsaturated reinforced slopes with nonwoven geotextile drains sandwiched in sand layers. Geosynth. Int. 22 (6), 457–474.
Unnikrishnan, N., Rajagopal, K., Krishnaswamy, N.R., 2002. Behaviour of reinforced clay under monotonic and cyclic loading. Geotext. Geomembranes 20 (2), 117–133.
Vahedifard, F., Mortezaei, K., Leshchinsky, B.A., Leshchinsky, D., Lu, N., 2016. Role of suction stress on service state behavior of geosynthetic-reinforced soil structures. Transportation Geotechnics 8, 45–56.
Vahedifard, F., Tehrani, F.S., Galavi, V., Ragno, E., AghaKouchak, A., 2017. Resilience of MSE walls with marginal backfill under a changing climate: quantitative assessment for extreme precipitation events. J. Geotech. Geoenviron. Eng. 143 (9).
Valentine, R.J., 2013. An assessment of the factors that contribute to the poor performance of geosynthetic-reinforced earth retaining walls. Proceeding of, International Symposium on Design and Practice of Geosynthetic-Reinforced Soil Structures 318–327. PA.
Viswanadham, B.V.S., König, D., 2004. Studies on scaling and instrumentation of a geogrid. Geotext. Geomembranes 22 (5), 307–328.
Viswanadham, B., Razeghi, H.R., Mamaghanian, J., Manikumar, C., 2017. Centrifuge model study on geogrid reinforced soil walls with marginal backfills with and without chimney sand drain. Geotext. Geomembranes 45 (5), 430–446.
WSDOT, 2005. *Geotechnical design manual*. M 46-03. In: Retaining Walls, and Reinforced Slopes. Washington State Department of Transportation, Olympia, Washington, USA (Chapter 15) Abutments.
Wu, J.Y., Chou, N.N., 2013. Forensic studies of geosynthetic reinforced structure failures. J. Perform. Constr. Facil. 27 (5), 604–613.
Wu, J.Y., Tang, A.H., 2008. Wetting-induced Geosynthetic Reinforced Slope Failure. *Proceedings of the 4th Asian Regional Conferernce on Geosynthetics*, Shanghai, China, pp. 229–233.
Yang, K.H., Zornberg, J.G., Liu, C.N., Lin, H.D., 2012. Stress distribution and development within geosynthetic-reinforced soil slopes. Geosynthetics Int. 19 (1), 62–78.
Yang, K.-H., Yalew, W.M., Nguyen, M.D., 2016. Behavior of geotextile-reinforced clay with a coarse material sandwich technique under unconsolidated-undrained triaxial compression. Int. J. GeoMech. 16 (3), 04015083.
Yang, K.-H., Thuo, J.N., Huynh, V.D.A., Nguyen, T.S., Portelinha, F.H.M., 2018. Numerical evaluation of reinforced slopes with various backfill-reinforcement-drainage systems subject to rainfall infiltration. Comput. Geotech. 96, 25–39.
Yang, K.H., Thuo, J.N., Chen, J.W., Liu, C.N., 2019a. Failure investigation of a geosynthetic-reinforced soil slope subjected to rainfall. Geosynth. Int. 26 (1), 42–65.
Yang, K.-H., Nguyen, T.S., Lee, Y.-H., Leshchinsky, B., 2019b. Performance and design of geosynthetic-reinforced soil slopes against rainfall: considering regional hydrological conditions. Geosynth. Int. 26 (5), 451–473.
Yang, K.-H., Chiang, J., Lai, Z.-W., Han, J., Lin, M.-L., 2020. Performance of geosynthetic- reinforced soil foundations across a normal fault. Geotext. Geomembranes 48 (3), 357–373.
Yasuhara, K., Recio-Molina, J., 2007. Geosynthetic-wrap around revetments for shore protection. Geotext. Geomembranes 25 (4–5), 221–232.
Yoo, C., Jang, D., 2013. Geosynthetic reinforced soil wall performance under heavy rainfall. Proceedings of the 18th International Conference on Soil Mechanics and Geotechnical Engineering: Challenges and Innovations in Geotechnics (Paris, France).
Yoo, C., Jung, H., 2006. Case history of geosynthetic reinforced segmental retaining wall failure. J. Geotech. Geoenviron. Eng. 132 (12), 1538–1548.
Yoo, C., Tabish, J.W., Yang, Q., Abbas, J.S., Song, S., 2022. Effect of internal draiange on deformation behavior of GRS wall during rainfall. Geosynth. Int. 29 (2), 137–150.
Zornberg, J.G., Arriaga, F., 2003. Strain distribution within geosynthetic-reinforced slopes. *Journal of Geotechnical and Geoenvironmental Engineering*, ASCE 129 (1), 32–45.